

Quadrupole partial orders and triple- \mathbf{q} states on the face-centered cubic lattice

Kazumasa Hattori and Takayuki Ishitobi
*Department of Physics, Tokyo Metropolitan University,
 1-1, Minami-osawa, Hachioji, Tokyo 192-0397, Japan*

Hirokazu Tsunetsugu
The Institute for Solid State Physics, The University of Tokyo, Kashiwanoha 5-1-5, Chiba 277-8581, Japan
 (Dated: July 6, 2023)

We study Γ_3 quadrupole orders in a face-centered cubic lattice. The Γ_3 quadrupole moments under cubic symmetry possess a unique cubic invariant in their free energy in the uniform ($\mathbf{q} = \mathbf{0}$) sector and the triple- \mathbf{q} sector for the X points $\mathbf{q} = (2\pi, 0, 0)$, $(0, 2\pi, 0)$, and $(0, 0, 2\pi)$. Competition between this cubic anisotropy and anisotropic quadrupole-quadrupole interactions causes a drastic impact on the phase diagram both in the ground state and at finite temperatures. We show details about the model construction and its properties, the phase diagram, and the mechanism of the various triple- \mathbf{q} quadrupole orders reported in our preceding letter [J. Phys. Soc. Jpn. **90**, 43701 (2021)]. By using a mean-field approach, we analyze a quadrupole exchange model that consists of a crystalline-electric field scheme with the ground-state Γ_3 non-Kramers doublet and the excited singlet Γ_1 state. We have found various triple- \mathbf{q} orders in the four-sublattice mean-field approximation. A few partially ordered phases are stabilized in a wide range of parameter space and they have a higher transition temperature than single- \mathbf{q} orders. With lowering temperature, there occur transitions from these partially ordered phases into further symmetry broken phases in which previously disordered sites acquire nonvanishing quadrupole moments. The identified phases in the mean-field approximation are further analyzed by a phenomenological Landau theory. This analysis reveals results qualitatively consistent with the mean-field results and also shows that the cubic invariant plays an important role for stabilizing the triple- \mathbf{q} states. The present mechanism for the triple- \mathbf{q} states also takes effect in systems with different types of quadrupoles, and we discuss its implications for recent experiments in a few f - and d -electron compounds.

I. INTRODUCTION

Strongly correlated electron systems possess a variety of possibilities of exotic phenomena [1, 2] and also innovative devices in future [3]. Strong correlations between d - or f -electrons often lead to fascinating and mysterious ordered phases [4], phase transitions [5], and even liquid like phases [2]. In addition to these correlation effects, the importance of spin-orbit (SO) coupling has been recognized for materials including heavy elements with $5d$ or $4d$ electrons [6–8]. These electrons are subject to both the crystalline-electric field (CEF) and the SO coupling. Various phenomena of multipoles emerge in such configurations [9]. This causes nontrivial properties in their spin, orbital, or more general multipole models [9, 10].

Several years ago, the present authors studied antiferro quadrupole orders in Pr 1-2-20 compounds [11–13], in which Pr ions form a diamond sublattice. Each Pr^{3+} ion has two f -electrons and its ground state is a non-Kramers doublet Γ_3 in the cubic environment, which is a consequence of the interplay of CEF and SO couplings [14]. This Γ_3 doublet has two active components of electric quadrupole O_{20} and O_{22} , and they form a two-dimensional basis of E irreducible representation of the cubic point group $\mathbf{Q}=(Q_u, Q_v)=(O_{20}, \sqrt{3}O_{22})$. To understand quadrupole orders in this system, it is too naive to make predictions based on the understanding of an apparently similar spin-1/2 model on the same lattice. Despite their local degrees of freedom being a doublet in common, there exists a crucial difference. This is due

to their opposite parities under time reversal operation: spin has odd parity, while electric quadrupole has even parity. Its even parity protects the presence of a nonvanishing third-order term of quadrupole moments in the system's free energy. Its consequences and implications were briefly discussed in the previous study [15].

More recently, Kusanose *et al.* have measured the low-temperature properties of Γ_3 quadrupole moments in another compound PrMgNi_4 [16–18]. An important difference is that Pr ions form a face-centered cubic (fcc) sublattice there. In our preceding study [15], we have shown that different lattice structures open a way to stabilize novel triple- \mathbf{q} orders including partial-ordered states. One can understand this by noting that the third-order term in the free energy contains a following coupling of the moments at three wavevectors $\mathbf{p}_{1,2,3}$,

$$\sim b_{ABC}A(\mathbf{p}_1)B(\mathbf{p}_2)C(\mathbf{p}_3), \quad (1)$$

with b_{ABC} being the third-order coupling constant. A requirement exists such that $\mathbf{p}_1 + \mathbf{p}_2 + \mathbf{p}_3 = \mathbf{G}$ should be one of the reciprocal lattice vectors. The set of $A(\mathbf{p}_1)$, $B(\mathbf{p}_2)$, and $C(\mathbf{p}_3)$ is a certain combination of multipole operators such that the product ABC remains invariant under any point-group symmetry operation. As the third-order coupling is nonvanishing $b_{ABC} \neq 0$, one naively expects a first-order transition occurring at a temperature higher than the second-order one, which is determined as a vanishing point of the second-order coefficient in the free energy. Such a type of third-order term has been discussed in several contexts for nonmagnetic systems including

the γ - α transition in Ce [19], possible low-temperature phases in UPd₃ [20], and multiple phases in PrV₂Al₂₀ [21]. As for the simplest cases with $\mathbf{p}_1 = \mathbf{p}_2 = \mathbf{p}_3 = \mathbf{0}$, quadrupole orders in PrTi₂Al₂₀ have been theoretically discussed [11, 12, 22–24], and also experimentally explored [25–28]. A system with Γ_3 quadrupole moments on an fcc lattice is the simplest realization for such triple- \mathbf{q} physics and we will study this in this paper in more detail than in the previous report [15].

This paper is organized as follows. In Sec. II, we will introduce a low-energy effective model defined in the space of Γ_3 and Γ_1 CEF states relevant to the Pr-based systems. We will explain the basic properties of exchange interactions between the quadrupole moments, and in Sec. III, we will examine the local quadrupole Hamiltonian. In Sec. IV, we will perform a single-site mean-field analysis for a Γ_3 -only model, and find that its results turn out insufficient. Then, we will proceed to the discussions about the four-site mean-field approximations including various triple- \mathbf{q} orders in Sec. V. Sections VI–VIII are devoted to phenomenological analyses of the microscopic mean-field results and we will clarify how various triple- \mathbf{q} orders including partially ordered states emerge. We will also discuss a possible application of the present triple- \mathbf{q} mechanism to other systems in Sec. IX and summarize this paper in Sec. X.

II. MODEL

In this section, we will introduce a model Hamiltonian to be studied in this paper for discussing quadrupole orders in Pr-based Γ_3 systems. In Sec. II A, we will analyze their local Hilbert space and construct an effective exchange Hamiltonian of f -electron quadrupoles based on their symmetry property. In Sec. II B, we will then analyze this exchange Hamiltonian at the classical level and carry out a mode analysis to identify the leading ordering patterns. One should understand that the quadrupole interactions are determined by integrating out the degrees of freedom of conduction electrons in the real Pr-based compounds, and we do not consider those conduction electrons explicitly. This is because our aim is to study the physics related to symmetry breakings exhibited by the localized f -electrons. Whether the system is insulating or metallic does not alter the qualitative aspect of the symmetry breaking. Exceptions are some details at quantum critical points [29], but they are not the issue of the present study. In order to determine the phase diagram and identify ordering patterns in each phase, the localized electron model is sufficient and has been used as a reasonable starting point in the studies of, e.g., CeB₆ [30, 31], URu₂Si₂ [32], and Pr 1-2-20 systems [23, 24]. Throughout this paper, we analyze fundamental properties of quadrupole orders in the minimal Γ_3 model (10) on the fcc lattice with the simplest fcc nearest-neighbor interactions and clarify their general trends with a few important material parameters rather

than focus on a specific material.

A. $\Gamma_3 - \Gamma_1$ model

We first explain the local Hilbert space of the Γ_3 systems for discussing quadrupole orders in their ground state systems. As discussed in Refs. [11, 12, 15], it is important to include the excited Γ_1 state in order to take into account local anisotropy. This is because the quadrupole operators have quite large matrix elements connecting the Γ_3 doublet to the Γ_1 state. See Eq. (5). The other CEF excited states can be safely neglected, since they have no quadrupole matrix elements with Γ_3 . Thus, our local Hilbert space consists of the singlet $\Gamma_1 = \{|s\rangle\}$ and the non-Kramers doublet $\Gamma_3 = \{|u\rangle, |v\rangle\}$:

$$|s\rangle = \frac{1}{\sqrt{12}} \left[\sqrt{\frac{5}{2}} (|4\rangle + |-4\rangle) + \sqrt{7} |0\rangle \right], \quad (2)$$

$$|u\rangle = \frac{1}{\sqrt{12}} \left[\sqrt{\frac{7}{2}} (|4\rangle + |-4\rangle) - \sqrt{5} |0\rangle \right], \quad (3)$$

$$|v\rangle = \frac{1}{\sqrt{2}} (|2\rangle + |-2\rangle). \quad (4)$$

Here $|J_z\rangle$ denotes the eigenstate of the z -component of the total angular momentum J_z in the multiplet of the total angular momentum $J=4$. Using these three basis states $\{|s\rangle, |u\rangle, |v\rangle\}$, the Γ_3 quadrupole operators $\mathbf{Q} \equiv (Q_u, Q_v)^T$ with T being the transpose are represented as [11]

$$Q_u \equiv \begin{pmatrix} 0 & \alpha & 0 \\ \alpha & 1 & 0 \\ 0 & 0 & -1 \end{pmatrix}, \quad Q_v \equiv \begin{pmatrix} 0 & 0 & \alpha \\ 0 & 0 & -1 \\ \alpha & -1 & 0 \end{pmatrix}, \quad \alpha \equiv \frac{\sqrt{35}}{2}. \quad (5)$$

As noted before, the matrix elements connecting Γ_3 to Γ_1 are quite large $\alpha \sim 3$.

In the fcc lattice, each site has twelve nearest neighbors separated by $\delta_{1,4} = (0, \frac{1}{2}, \pm\frac{1}{2})$, $\delta_{2,5} = (\mp\frac{1}{2}, 0, \frac{1}{2})$, $\delta_{3,6} = (\frac{1}{2}, \pm\frac{1}{2}, 0)$, and their counterparts $-\delta$'s. See Fig. 1. The symmetry analysis in our previous study concluded that quadrupole interactions generally have anisotropic couplings in addition to isotropic ones [15]. The minimal model of quadrupole interactions reads as

$$H_Q = \sum_{\langle \mathbf{r}, \mathbf{r}' \rangle} \mathbf{Q}(\mathbf{r}) \cdot \mathbf{J}_{\mathbf{r}-\mathbf{r}'} \mathbf{Q}(\mathbf{r}'), \quad (6)$$

$$\mathbf{J}_{\mathbf{r}-\mathbf{r}'} = J\mathbf{g}_0 + K\mathbf{g}(\mathbf{r}-\mathbf{r}'), \quad (7)$$

where $\langle \mathbf{r}, \mathbf{r}' \rangle$ indicates that the sum runs over the nearest-neighbor site pairs and $\mathbf{g}_0 = \hat{\sigma}_0$. Throughout this paper, $\hat{\sigma}_0$ denotes the 2×2 identity matrix. The anisotropy factor has a form represented with the Pauli matrices $\hat{\sigma}_1$ and $\hat{\sigma}_3$

$$\mathbf{g}(\boldsymbol{\delta}) = \cos \zeta(\boldsymbol{\delta}) \hat{\sigma}_3 - \sin \zeta(\boldsymbol{\delta}) \hat{\sigma}_1, \quad (8)$$

where $\hat{\sigma}_{1,3}$ operate in the (Q_u, Q_v) space. The angle parameter $\zeta(\boldsymbol{\delta})$ is defined for the bond vector $\boldsymbol{\delta} = (x, y, z)$ as

$$\zeta(\boldsymbol{\delta}) = \text{Im} \log(e^{i\omega} x^2 + e^{-i\omega} y^2 + z^2), \quad \omega \equiv \frac{2}{3}\pi. \quad (9)$$

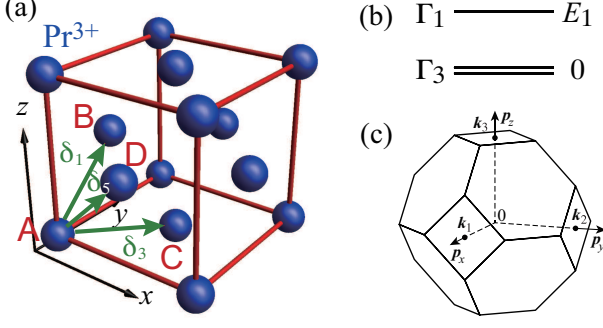


FIG. 1. (a) Cubic unit cell of the fcc lattice of Pr ions and its four sublattices labeled by A-D. $\vec{AB}=\delta_1$, $\vec{AC}=\delta_3$, and $\vec{AD}=\delta_5$. (b) The relevant CEF states of a Pr^{3+} ion in this paper. Γ_3 is the non-Kramers ground-state doublet and Γ_1 is a singlet excited state. $|m\rangle$ is the eigenstate $J_z|m\rangle = m|m\rangle$ in the $J=4$ multiplet. (c) Brillouin zone of the fcc lattice. The three X points are $\mathbf{k}_1=(2\pi,0,0)$, $\mathbf{k}_2=(0,2\pi,0)$, and $\mathbf{k}_3=(0,0,2\pi)$.

As for the nearest-neighbor bonds, $\zeta(\pm\delta_n)=n\omega-\pi$, and this leads to the relation $\mathbf{g}(\delta_1)+\mathbf{g}(\delta_3)+\mathbf{g}(\delta_5)=0$. The same type of anisotropic coupling has been used in the so-called compass model to study orbital orders [33]. The effective model (6) was obtained with the special value $K=J$ by Kubo and Hotta starting from a microscopic electron Hamiltonian [34]. The special K value is due to a simple form of their microscopic Hamiltonian, and various other types of super-exchange processes generate $K \neq J$.

We also note that, conduction electrons cause the RKKY interactions between the localized quadrupole moments. The RKKY interactions have, in general, a longer range beyond the nearest-neighbor distance used in this paper. However, their range remains finite at finite temperatures, since electron propagation loses long-range coherence due to thermal fluctuations. The distance dependence of the RKKY interactions is quite complicated and one needs to consider the details of the Fermi surfaces to calculate its dependence. Before performing that type of elaborate calculation, we have to clarify fundamental features of quadrupole orders and focus on a minimal model in which conduction electron degrees of freedom are traced out.

We denote by E_1 the Γ_1 energy level relative to the Γ_3 's value, and assume $E_1 > 0$ throughout this paper. Then, we define the Hamiltonian of the Γ_3 - Γ_1 model by

$$H = E_1 \sum_{\mathbf{r}} |s(\mathbf{r})\rangle \langle s(\mathbf{r})| + H_Q. \quad (10)$$

In the following sections, we will analyze in detail the exchange interactions H_Q and the properties of a single-site Hamiltonian under quadrupolar molecular fields.

B. Exchange interactions

Let us start with finding a classical ground state based on the Fourier mode analysis of H_Q . In terms of Fourier components $\mathbf{Q}_{\mathbf{p}} = N^{-1/2} \sum_{\mathbf{r}} e^{-i\mathbf{p} \cdot \mathbf{r}} \mathbf{Q}(\mathbf{r})$ (N is the number of sites), H_Q is represented as

$$H_Q = \sum_{\mathbf{p}} \mathbf{Q}_{\mathbf{p}} \cdot \mathbf{J}(\mathbf{p}) \mathbf{Q}_{-\mathbf{p}}, \quad (11a)$$

$$\mathbf{J}(\mathbf{p}) \equiv \sum_{n=1}^6 e^{i\mathbf{p} \cdot \delta_n} \mathbf{J}_{\delta_n} = J\gamma_0(\mathbf{p})\hat{\sigma}_0 + K\gamma(\mathbf{p}), \quad (11b)$$

where the sum $\sum_{\mathbf{p}}$ is taken over the wavevectors in the Brillouin zone (BZ) shown in Fig. 1(c). The coupling constants are given by

$$\gamma_{n=0,1}(\mathbf{p}) \equiv 2[c_{xy}(\mathbf{p}) + e^{in\omega}c_{yz}(\mathbf{p}) + e^{-in\omega}c_{zx}(\mathbf{p})], \quad (11c)$$

$$\begin{aligned} \gamma(\mathbf{p}) &= -[\text{Re } \gamma_1(\mathbf{p})] \hat{\sigma}_3 + [\text{Im } \gamma_1(\mathbf{p})] \hat{\sigma}_1 \\ &= [-\tfrac{1}{2}\gamma_1(\mathbf{p})(\hat{\sigma}_3 + i\hat{\sigma}_1)] + \text{h.c.}, \end{aligned} \quad (11d)$$

and the form factor $c_{ab}(\mathbf{p})$ is defined as

$$c_{ab}(\mathbf{p}) \equiv \cos(\tfrac{1}{2}p_a) \cos(\tfrac{1}{2}p_b). \quad (11e)$$

Note that $\mathbf{J}(\mathbf{p}) = \mathbf{J}(-\mathbf{p})$ is a real symmetric matrix, and this guarantees the hermicity of H_Q .

A classical ground state is a spiral state, and its propagating vector $\mathbf{p}=\mathbf{q}_*$ is the position where the coefficient matrix $\mathbf{J}(\mathbf{p})$ has the maximally negative eigenvalue. The diagonalization of $\mathbf{J}(\mathbf{p})$ is straightforward and the eigenvalues are

$$\Lambda_{\mp}(\mathbf{p}) = J\gamma_0(\mathbf{p}) \mp K|\gamma_1(\mathbf{p})|. \quad (12)$$

In terms of the notation introduced for a unit vector pointing to the direction of angle θ

$$\hat{\mathbf{e}}_{\theta} \equiv (\cos \theta, \sin \theta)^T =: \hat{\mathbf{e}}(\theta), \quad (13)$$

the corresponding eigenvectors are written as

$$\mathbf{v}_-(\mathbf{p}) = \hat{\mathbf{e}}(\vartheta_{\mathbf{p}}), \quad \mathbf{v}_+(\mathbf{p}) = \hat{\mathbf{e}}(\vartheta_{\mathbf{p}} + \pi/2), \quad (14)$$

for $\Lambda_-(\mathbf{p})$ and $\Lambda_+(\mathbf{p})$, respectively. The angle parameter $\vartheta_{\mathbf{p}}$ is given by the following parametrization:

$$\gamma_1(\mathbf{p}) = |\gamma_1(\mathbf{p})| e^{-2i\vartheta_{\mathbf{p}}}, \quad \vartheta_{\mathbf{p}}: \text{real}. \quad (15)$$

Figure 2 shows the eigenvalues $\Lambda_{\mp}(\mathbf{p})$ in the p_x - p_y plane for $J < 0$ as an illustrative example.

We can easily show that the maximally negative eigenvalue is

$$\Lambda_{\min} = \begin{cases} -2J - 4|K| & \text{for } |K| + 2J > 0 \\ 6J & \text{for } 2J < |K| < -2J \end{cases}. \quad (16)$$

The minimum position is located at $\mathbf{k}_1=(2\pi,0,0)$, $\mathbf{k}_2=(0,2\pi,0)$, and $\mathbf{k}_3=(0,0,2\pi)$ when $|K| + 2J > 0$,

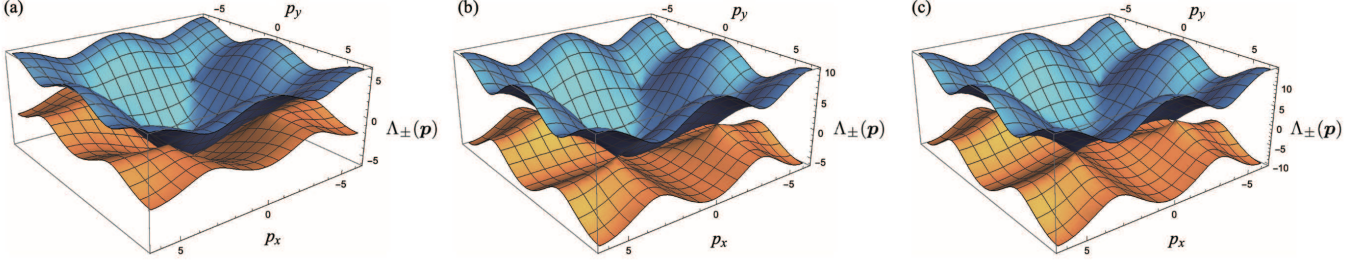


FIG. 2. The eigenvalues $\Lambda_{\pm}(\mathbf{p})$ in the p_x - p_y plane for $J < 0$. $K/|J| =$ (a) 1.0, (b) 2.0, and (c) 3.0. Note that $(2\pi, 2\pi, 0) \equiv (0, 0, 2\pi)$ for the fcc lattice

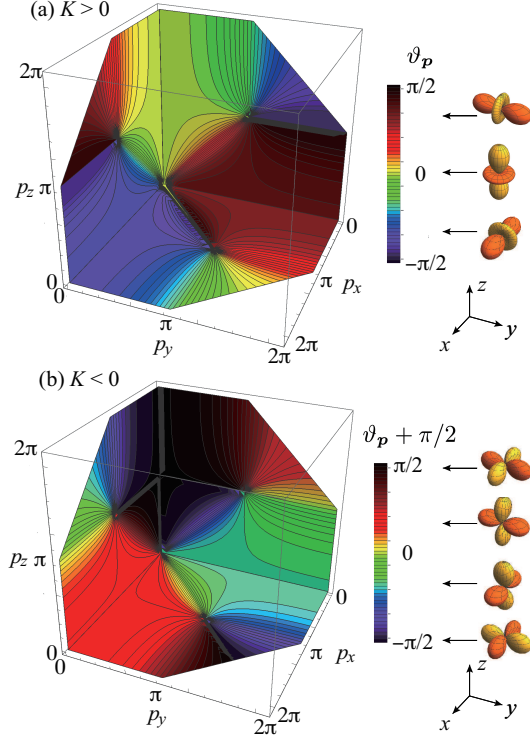


FIG. 3. $\vartheta_{\mathbf{p}}$ in the p_x - p_y , p_y - p_z , and p_z - p_x planes. Shown are (a) $\vartheta_{\mathbf{p}}$ for $K > 0$ and (b) $\vartheta_{\mathbf{p}} + \pi/2$ for $K < 0$. When the angle $|\vartheta_{\mathbf{p}}|$ or $|\vartheta_{\mathbf{p}} + \pi/2|$ exceeds $\pi/2$, it is shifted by π to an equivalent value. In (a), the eigenvectors at the X points are those with $\vartheta_{\mathbf{k}_1} = \bar{\vartheta}(\mathbf{k}_1) = -\pi/3$, $\vartheta_{\mathbf{k}_2} = \bar{\vartheta}(\mathbf{k}_2) = \pi/3$, and $\vartheta_{\mathbf{k}_3} = \bar{\vartheta}(\mathbf{k}_3) = 0$, where schematic u -type orbital shapes are illustrated. In (b), $\vartheta_{\mathbf{k}_1} = \bar{\vartheta}(\mathbf{k}_1) = \pi/6$, $\vartheta_{\mathbf{k}_2} = \bar{\vartheta}(\mathbf{k}_2) = -\pi/6$, and $\vartheta_{\mathbf{k}_3} = \bar{\vartheta}(\mathbf{k}_3) = \pi/2$ or equivalently $-\pi/2$.

while at $\mathbf{k}_0 = (0, 0, 0)$ otherwise. Thus, the propagating wavevector \mathbf{q}_* is either one of $\mathbf{k}_{1,2,3}$ or \mathbf{k}_0 depending on the parameters. Note that $\mathbf{k}_{1,2,3}$ are the X points in the BZ, i.e., the centers of the three pairs of square parts on the BZ surface. See Fig. 1(c). When $J < 0$ and $|K| < 2|J|$, one expects a ferro order in the ground state.

The eigenvector $\mathbf{u}(\mathbf{q}_*)$ of the maximally negative eigenvalue Λ_{\min} describes the unstable mode that orders at a phase transition approaching from the paramagnetic

phase side, and the local ordered moments are given as $\langle \mathbf{Q}(\mathbf{r}) \rangle = \text{Re} \mathbf{u}(\mathbf{q}_*) e^{i\mathbf{q}_* \cdot \mathbf{r}}$. For the ferro ordering, the coefficient matrix $\mathbf{J}(\mathbf{k}_0) = 6J\hat{\sigma}_0$ is isotropic and thus the order parameter $\langle \mathbf{Q} \rangle$ may point to any direction in the quadrupole space within the level of Fourier mode analysis.

In the following parts of this paper, we concentrate on “antiferro” orders with the ordering wavevector $\mathbf{k}_{\ell \neq 0}$ in detail. The eigenvector $\mathbf{u}(\mathbf{q}_*)$ is $\mathbf{v}_-(\mathbf{q}_*)$ for $K > 0$, and $\mathbf{v}_+(\mathbf{q}_*)$ for $K < 0$, and let us represent as $\mathbf{u}(\mathbf{q}_*) = (\cos \bar{\vartheta}(\mathbf{q}_*), \sin \bar{\vartheta}(\mathbf{q}_*))^T$ for both cases. Then, its direction is given as

$$\bar{\vartheta}(\mathbf{q}_* = \mathbf{k}_{\ell}) = \begin{cases} K > 0 & K < 0 \\ \frac{7}{6}\pi \mp \frac{1}{2}\pi, & \frac{2}{3}\pi \pm \frac{1}{2}\pi & \text{at } \mathbf{k}_1 \\ \frac{5}{6}\pi \pm \frac{1}{2}\pi, & \frac{4}{3}\pi \pm \frac{1}{2}\pi & \text{at } \mathbf{k}_2. \\ \frac{1}{2}\pi \mp \frac{1}{2}\pi, & \pi \mp \frac{1}{2}\pi & \text{at } \mathbf{k}_3 \end{cases} \quad (17)$$

See Fig. 3. For example, the order with $\mathbf{q}_* = \mathbf{k}_3$ has the order parameter $\langle \mathbf{Q}(\mathbf{r}) \rangle = (-1)^{2z} (Q_u, 0)^T$ for $K > 0$, while $(-1)^{2z} (0, Q_v)^T$ for $K < 0$. They are known as O_{20} - and O_{22} -type AFQ order, respectively. Note that for a more general order parameter, the cubic lattice symmetry implies that generally six values of the order parameters

$$\langle \mathbf{Q} \rangle = q\hat{e}(0) \pm q'\hat{e}(\frac{\pi}{2}), \quad q\hat{e}(\omega) \pm q'\hat{e}(\omega + \frac{\pi}{2}), \quad (18) \\ q\hat{e}(-\omega) \pm q'\hat{e}(-\omega + \frac{\pi}{2}),$$

are equivalent. They are related to two types of lattice symmetry operations: one is a $\frac{1}{2}\pi$ rotation about one of the three principle axes $R_i(\pm\frac{1}{2}\pi)$ ($i = x, y, z$), and the other is an ω rotation about the axis along $[1, 1, 1]$ direction $R_1(\pm\omega)$. The above six $\langle \mathbf{Q} \rangle$ values are transformed from one to another by these operations.

We emphasize that the phase factor of the eigenvectors $\mathbf{u}(\mathbf{k}_{\ell})$ are not relevant in this Fourier mode analysis. However, they play a role at the stage that mode couplings are taken into account.

III. SINGLE-SITE PROPERTY

For discussing possible phases and their transitions in this system, it is important to first understand

single-site properties under quadrupole molecular field $\mathbf{h}=(h_u, h_v)^T$. It turns out that the wavefunction changes its topological character as the field strength grows, and this change is reflected in the phase diagrams of interacting quadrupoles.

A single-site Hamiltonian is given as

$$\mathcal{H}_{\text{mf}} = -\mathbf{h} \cdot \mathbf{Q} + E_1 |s\rangle\langle s|, \quad (19)$$

where the site label \mathbf{r} is omitted. As for the external fields, only those coupled to \mathbf{Q} are considered here, since our concern in this paper is quadrupole orders. Since multiplying a positive factor to \mathcal{H}_{mf} does not change its ground state, we normalize the Hamiltonian such that $\mathbf{h}^2 + E_1^2 = 1$ and introduce the polar coordinates defined by

$$(h_u, h_v) = \sin \Theta (\cos \Phi, \sin \Phi), \quad E_1 = \cos \Theta. \quad (20)$$

The normalized Hamiltonian is now represented as

$$\begin{aligned} \mathcal{H}_{\text{mf}} &= \mathcal{H}_{\text{mf}}(\Theta, \Phi) \\ &= \begin{pmatrix} \cos \Theta & -\alpha \sin \Theta \cos \Phi & -\alpha \sin \Theta \sin \Phi \\ -\alpha \sin \Theta \cos \Phi & -\sin \Theta \cos \Phi & \sin \Theta \sin \Phi \\ -\alpha \sin \Theta \sin \Phi & \sin \Theta \sin \Phi & \sin \Theta \cos \Phi \end{pmatrix}. \end{aligned} \quad (21)$$

Our primary concern is about the case of $0 < \Theta \leq \frac{1}{2}\pi$, and there exists the symmetry $\mathcal{H}_{\text{mf}}(\pi - \Theta, \pi + \Phi) = -\mathcal{H}_{\text{mf}}(\Theta, \Phi)$.

It is important to understand the symmetry of this Hamiltonian that is related to the cubic lattice structure. Let R be one of the aforementioned two types of rotation operators. Its application transforms a wavefunction with an orthogonal matrix as $\psi' = \mathcal{U}_R \psi$, and thus the Hamiltonian is correspondingly transformed as $\mathcal{H}'_{\text{mf}} = \mathcal{U}_R \mathcal{H}_{\text{mf}} \mathcal{U}_R^T$. The transformation matrices for $R=R_z(\pm\pi/2)$ and $R_1(\pm\omega)$ are $\mathcal{U}_R = \mathcal{M}_z = \mathcal{M}(0)$ and $\mathcal{U}(\pm\omega)$, respectively, in terms of the notations defined for general θ by

$$\mathcal{M}(\theta) = \begin{pmatrix} 1 & 0 & 0 \\ 0 & \cos \theta & -\sin \theta \\ 0 & -\sin \theta & -\cos \theta \end{pmatrix} = 1 \oplus \mu(\theta), \quad (22a)$$

$$\mathcal{U}(\theta) = \begin{pmatrix} 1 & 0 & 0 \\ 0 & \cos \theta & -\sin \theta \\ 0 & \sin \theta & \cos \theta \end{pmatrix} = 1 \oplus U(\theta), \quad (22b)$$

where $\mu(\theta)$ and $U(\theta)$ are 2×2 orthogonal matrices operating in the Γ_3 subspace. Note that the Γ_1 space is invariant for any R , since it is singlet. $\mu(\theta)$ is a mirror operator in the Γ_3 multiplet. The other symmetry operations of $\theta = \pm\frac{1}{2}\pi$ rotations can be represented as $R_x(\theta) = R_1(\omega)R_z(\theta)R_1(-\omega)$ and $R_y(\theta) = R_1(-\omega)R_z(\theta)R_1(\omega)$. The corresponding mirrors are given as $\mathcal{M}_{x,y} = \mathcal{U}(\pm\omega)\mathcal{M}_z\mathcal{U}(\mp\omega) = \mathcal{M}(\pm\omega)$. Note the relations $[\mathcal{U}(n\omega)]^T = \mathcal{U}(-n\omega)$ and $\mathcal{M}(n\omega)\mathcal{M}(n'\omega) = \mathcal{U}((n'-n)\omega)$.

Now that the transformation matrices are obtained, we can directly show that the transformed Hamiltonian also has the form of $\mathcal{H}_{\text{mf}}(\Theta, \Phi')$ and the new field direction Φ' is determined. The result is summarized as follows:

$$\mathcal{U}(n\omega) \mathcal{H}_{\text{mf}}(\Theta, \Phi) [\mathcal{U}(n\omega)]^T = \mathcal{H}_{\text{mf}}(\Theta, \Phi + n\omega), \quad (23a)$$

$$\mathcal{M}(n\omega) \mathcal{H}_{\text{mf}}(\Theta, \Phi) \mathcal{M}(n\omega) = \mathcal{H}_{\text{mf}}(\Theta, -\Phi - n\omega), \quad (23b)$$

for $n = 0, \pm 1$. Note that the transformations change Φ alone. These manifest the equivalence of the following six field directions

$$\Phi' = \pm(\Phi + n\omega), \quad (n = 0, \pm 1). \quad (24)$$

To be more precise, the Hamiltonians for these Φ 's are related to each other through orthogonal transformations. For the three special directions $\Phi = n\omega$ ($n = 0, \pm 1$), $[\mathcal{M}(\Phi), \mathcal{H}_{\text{mf}}(\Theta, \Phi)] = 0$, and therefore the ground state wavefunction should be a simultaneous eigenvector of $\mathcal{M}(\Phi)$. Finally, in the limit $\Theta \rightarrow 0$, the Γ_1 component of the ground state vanishes. The Hamiltonian projected to the remaining Γ_3 subspace $\mathcal{P}\mathcal{H}_{\text{mf}}\mathcal{P}$ has a continuous symmetry $\mathcal{P}\mathcal{H}_{\text{mf}}(0, \Phi)\mathcal{P} = U(\frac{1}{2}\Phi)[\mathcal{P}\mathcal{H}_{\text{mf}}(0, 0)\mathcal{P}][U(\frac{1}{2}\Phi)]^T$.

Let $\langle \mathbf{Q} \rangle_0(\Phi)$ be the ground-state expectation value calculated for $\mathcal{H}_{\text{mf}}(\Theta, \Phi)$, and then it is also accordingly transformed for the equivalent Φ 's in Eq. (24). For simplicity, we drop the Θ -dependence for a while. The relations (23) imply

$$\begin{aligned} \langle \mathbf{Q} \rangle_0(\Phi + n\omega) &= \langle [\mathcal{U}(n\omega)]^T \mathbf{Q} \mathcal{U}(n\omega) \rangle_0(\Phi) \\ &= U(n\omega) \langle \mathbf{Q} \rangle_0(\Phi), \end{aligned} \quad (25a)$$

$$\begin{aligned} \langle \mathbf{Q} \rangle_0(2n\omega - \Phi) &= \langle \mathcal{M}(n\omega) \mathbf{Q} \mathcal{M}(n\omega) \rangle_0(\Phi) \\ &= \mu(n\omega) \langle \mathbf{Q} \rangle_0(\Phi). \end{aligned} \quad (25b)$$

This means that the quadrupole moment $\langle \mathbf{Q} \rangle_0$ is transformed as a two-dimensional vector with the rotation $U(n\omega)$ or mirror $\mu(n\omega)$ operation defined in Eqs. (22). The transformed values are those six listed in Eq. (18). These symmetries also imply the following properties for the special field directions $\Phi = \frac{1}{2}\omega \times (\text{integer})$:

$$\langle \mathbf{Q} \rangle_0(\Phi) \parallel \mathbf{h}, \quad \frac{\partial}{\partial \Phi} |\langle \mathbf{Q} \rangle_0(\Phi)| = 0, \quad (26)$$

Let us analyze the eigenvalues of $\mathcal{H}_{\text{mf}}(\Theta, \Phi)$. It is enlightening to regard this problem as a one-dimensional system with three internal states where Φ is its “wave number” while Θ is a control parameter [35]. At $\Theta = \pi$, the ground state wavefunction is trivially a pure singlet Γ_1 state and the excitations are fully gapped for all Φ 's as shown in Fig. 4. As Θ decreases, the gap reduces and closes at $\Theta_c = \cot^{-1} \frac{27}{8} \simeq 0.092\pi$ and $\Phi = \pi + n\omega$ ($n = 0, \pm 1$). The symmetry of the Hamiltonian also implies a level crossing between the two excited states at $\Theta = \pi - \Theta_c$. With varying Θ , the ground state changes its nature drastically from a half-integer “spin” type ($\Theta \sim 0$) to an integer “spin” one ($\Theta > \Theta_c$).

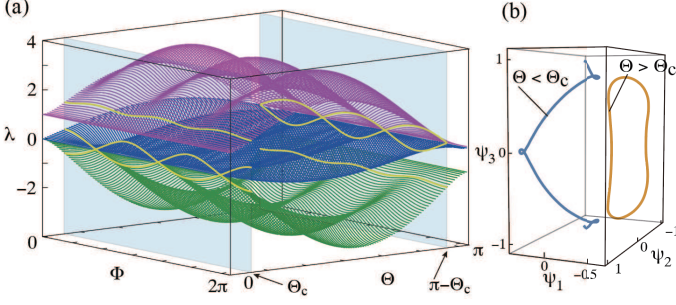


FIG. 4. (a) Eigenenergies λ of $\mathcal{H}_{mf}(\Theta, \Phi)$ in Eq. (21). For clarity, the data for $\Theta = \Theta_c$ or $\pi - \Theta_c$, showing the gap closing, are highlighted. (b) Trajectory of the ground state wavefunction $\psi = (\psi_1, \psi_2, \psi_3)$ from $\Phi = 0$ to 2π . The values with $\Theta = \cot^{-1} 5 < \Theta_c$ and $\Theta = \cot^{-1} 3 > \Theta_c$ are used as examples. $\psi_i(\Phi = 2\pi) = -\psi_i(0)$ for all i 's when $\Theta < \Theta_c$, while $\psi_i(2\pi) = \psi_i(0)$ when $\Theta > \Theta_c$. The upper and lower end points correspond to $\Phi = \pm\pi$ for $\Theta < \Theta_c$.

This change is characterized by the Berry phase factor $(-1)^{2\pi\chi_B}$ of the ground state wavefunction ψ acquired during the adiabatic change in Φ from 0 to 2π : $\psi(\Phi=2\pi) = (-1)^{2\pi\chi_B} \psi(0)$ [36, 37]. This factor $(-1)^{2\pi\chi_B}$ is -1 for $\Theta < \Theta_c$, while $+1$ for $\Theta > \Theta_c$. This change comes from the contribution of the three singular points at $(\Theta, \Phi) = (\Theta_c, \pi + n\omega)$, at which the two low-energy modes exhibit a dispersion of Dirac-cone type.

This change in the ground-state wavefunction is clearly reflected in the trajectory of quadrupole moment $\langle \mathbf{Q} \rangle_0(\Theta, \Phi) = [\psi(\Theta, \Phi)]^\dagger \mathbf{Q} \psi(\Theta, \Phi)$ upon varying Φ from 0 to 2π . See Figs. 5 and 6. The Φ -trajectory exhibits qualitatively different shapes in the four regions of Θ : (A) $0 \leq \Theta < \Theta_{c2} \equiv \cot^{-1} \frac{27}{4} \simeq 0.047\pi$, (B) $\Theta_{c2} < \Theta < \Theta_c$, (C) $\Theta_c < \Theta < \frac{1}{2}\pi$, (D) $\frac{1}{2}\pi < \Theta < \pi$. We will discuss each region below.

Let us start from the region A. Results for several values of $\Theta \leq \Theta_c$ are shown in Fig. 5. In the limit $\Theta \rightarrow 0$ (i.e., $|\mathbf{h}|/E_1 \rightarrow 0$), the ground state has no Γ_1 component, and thus can be represented as a pseudospin-1/2 wavefunction. This leads to trivial results: $|\langle \mathbf{Q} \rangle_0| = 1$ and $\langle \mathbf{Q} \rangle_0 \parallel \mathbf{h}$ for any field direction Φ . Thus, the Φ -trajectory is a unit circle. As Θ increases, the amplitude of $\langle \mathbf{Q} \rangle_0$ grows and its direction deviates from the field direction Φ . As a consequence, the trajectory is no longer circular but keeps threefold rotation and mirror symmetries imposed by the relations (25). This indicates that the hybridization of the Γ_1 state generates an anisotropy in the \mathbf{Q} space, and this is an essentially important aspect of the quadrupole order. The three special field directions $\Phi = \pi + n\omega$ ($n = 0, \pm 1$) are special, and the moment is then pinned as $\langle \mathbf{Q} \rangle_0(\Theta, \Phi) = (\cos \Phi, \sin \Phi)^T$ and does not change its amplitude with Θ . In their opposite directions $\Phi = n\omega$, the moment has a maximal amplitude

$$|\langle \mathbf{Q} \rangle_0(\Theta, n\omega)| = \frac{1}{2} \left[1 + \frac{\cot \Theta + 36}{\sqrt{(\cot \Theta + 1)^2 + 35}} \right], \quad (27)$$

and this value grows monotonically from 1 to $\frac{7}{2}$ as Θ varies from 0 to $\frac{1}{2}\pi$. The upper boundary of the region A is Θ_{c2} , and for the three special field directions the quadrupole moment points to

$$\langle \mathbf{Q} \rangle_0(\Theta_{c2}, n\omega) = \frac{35}{13} (\cos n\omega, \sin n\omega)^T =: \bar{\mathbf{Q}}_p^{(n)}. \quad (28)$$

These become cusps of the Φ -trajectory, and actually the Φ -dependence is singular there: for example, $\langle Q_v \rangle_0(\Theta_{c2}, \delta\Phi) \propto (\delta\Phi)^5$ for $|\delta\Phi| \ll 1$.

In the region B of Θ , the moment $\langle \mathbf{Q} \rangle_0$ changes its direction non-monotonically with Φ , and the trajectory has three pinch points located at $\bar{\mathbf{Q}}_p^{(n)}$. The pinch points are reached when the field direction is $\Phi = n\omega \pm \delta$ where $\cos \delta = \cot \Theta / \cot \Theta_{c2}$. It is remarkable that each pinch point $\bar{\mathbf{Q}}_p^{(n)}$ is visited *twice* upon varying field direction Φ with Θ fixed: once from “above” and from “below” the other time. See the inset of Fig. 5. These pinch points do not move with Θ in the region B, since the ground state there is fixed to $\psi(\Theta, n\omega \pm \delta) \propto \mathcal{U}(n\omega)(1, \alpha, 0)^T$.

The upper boundary of the region B is $\Theta = \Theta_c$, and this case is exceptional. The Φ -trajectory is not connected but consists of three disconnected parts. This is due to the level crossing of the ground state at $(\Theta_c, \Phi = \pi + n\omega)$ discussed before. The doubly degenerate ground states are $\psi_1 \propto \mathcal{U}(n\omega)(2, -\alpha, 0)^T$ and $\psi_2 = \mathcal{U}(n\omega)(0, 0, 1)^T$. With approaching one level-crossing point from some direction in the (Θ, Φ) space, these two states are hybridized to form the ground state as $\psi_1 \cos \xi + \psi_2 \sin \xi$, and the mixing angle ξ is determined by the approaching direction. With varying ξ for each crossing point, the expectation value $\langle \mathbf{Q} \rangle_0$ traces a fraction of an ellipse. For example, around the crossing point at $\Phi = \pi$ (i.e., $n=0$), this ellipse is expressed as

$$\left(\frac{\langle Q_u \rangle_0 + 26/17}{9/17} \right)^2 + \left(\frac{\langle Q_v \rangle_0}{\sqrt{105/17}} \right)^2 = 1. \quad (29)$$

One should note that the “pinned” point $\langle \mathbf{Q} \rangle_0 = (-1, 0)^T$ is on the minor axis of this ellipse. The ellipses for the other level crossing points are obtained by rotating this by the angle $\pm\omega$ about the origin. When the parameter set passes a level-crossing point $(\Theta_c, \Phi = \pi + n\omega)$, $\langle \mathbf{Q} \rangle_0$ jumps from one point on the corresponding ellipse to its opposite point. In the case of the Φ -trajectory, this jump takes place from a point on the ellipse's *major* axis to its opposite point. Thus, the interiors of these ellipses are a *forbidden region* of $\langle \mathbf{Q} \rangle_0$ as far as $E_1 > 0$, and this property is also important in the discussion of the quadrupole order.

In the region C of Θ , the Φ -trajectory becomes simple again. Just above Θ_c , $|\langle \mathbf{Q} \rangle_0|$ shows jumps to the larger magnitude as shown in Fig. 6(a). This is what we have just discussed above. For example, $|\langle \mathbf{Q} \rangle_0|(\Phi = \pi)$ jumps from 1 at $\Theta = \Theta_c - 0$ to $\frac{35}{17}$ at $\Theta_c + 0$. In this region, the quadrupole moment changes its direction monotonically with Φ as shown in Fig. 6(a).

Finally, while the region D ($\frac{1}{2}\pi < \Theta$) is not directly relevant to the following sections, we also study this region

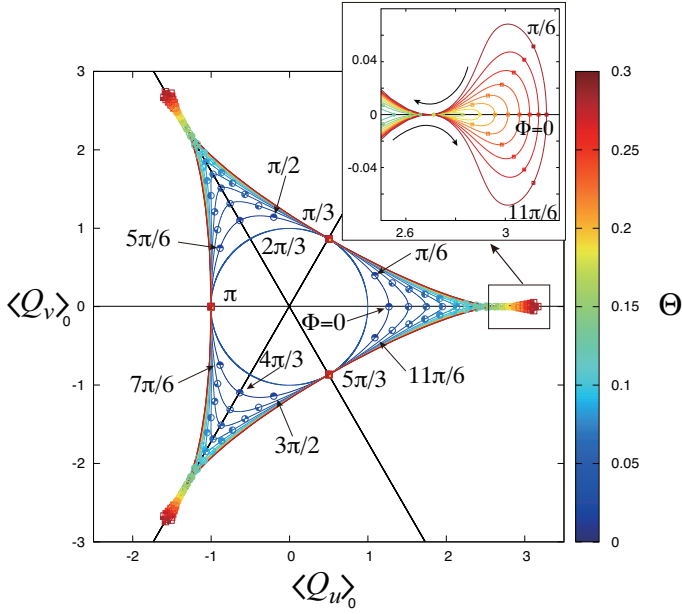


FIG. 5. Trajectory of $\langle \mathbf{Q} \rangle_0$ as Φ varies from 0 to 2π is drawn for several values of $\Theta < \Theta_c$. The Θ value is shown by color, and positions for typical Φ values are indicated. The unit circle represents the result in the pseudospin-1/2 limit ($\Theta = 0$). The magnitude $|\langle \mathbf{Q} \rangle_0|$ increases as Θ increases. Inset is a zoom up near $\langle \mathbf{Q} \rangle_0 \sim (3, 0)^T$ where $\Phi \sim 0$. The arrows indicate the direction for increasing Φ . Trajectories show a similar behavior for $\Phi \sim 2\pi/3$ and $4\pi/3$.

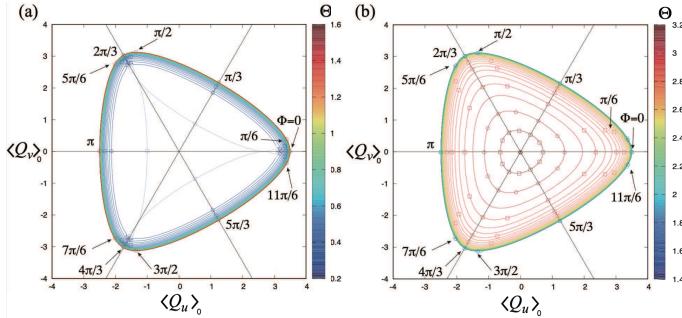


FIG. 6. Φ -trajectories of $\langle \mathbf{Q} \rangle_0$ for $\Theta \geq \Theta_c$. The magnitude $|\langle \mathbf{Q} \rangle_0|$ increases as Θ increases (a) when $\Theta < \pi/2$, while decreases when (b) $\pi/2 < \Theta < \pi$.

to complete the single-site analysis. This corresponds to the situation where the singlet Γ_1 level is below the Γ_3 doublet. This indicates that $|\langle \mathbf{Q} \rangle_0|$ should shrink to 0 as Θ approaches π . This process is shown in Fig. 6(b). The change is smooth with respect to both Θ and Φ , and shows no jump or singularity. This is consistent with the energy level analysis in Fig. 4(a), where there is no ground-state level crossing.

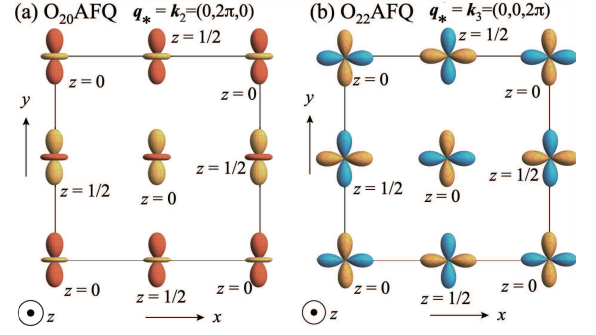


FIG. 7. Quadrupole configuration in the AFQ ordered states viewed from the positive z direction. The z coordinate of each site is indicated beside the orbital. (a) O_{20} AFQ order with $\mathbf{q}_* = \mathbf{k}_2$. (b) O_{22} AFQ order with $\mathbf{q}_* = \mathbf{k}_3$.

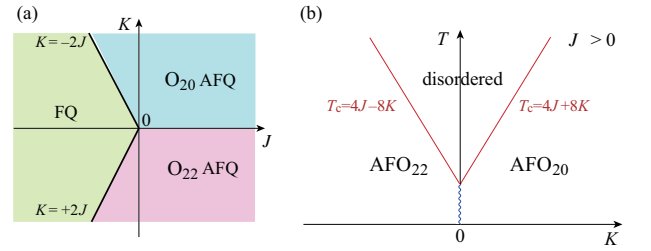


FIG. 8. Phase diagram in the limit of $E_1 \rightarrow \infty$ in (a) the J - K and (b) the K - T plane. In (b) the wavy line represents a first-order transition.

IV. MEAN FIELD APPROACH

In this section, we employ a mean-field approach to determine the phase diagram and investigate ordered phases. We will first analyze the limit of $E_1 \rightarrow \infty$. This corresponds to a pseudospin- $\frac{1}{2}$ model with no internal anisotropy. As shown in Fig. 5, the trajectory of field response is a unit circle, despite the anisotropic interaction K exists. We will show that only three states appear in that limit: two antiferro states with O_{20} or O_{22} order parameter, and an isotropic ferro state. Then, we will proceed to develop a four-sublattice mean-field theory. Its results predict several triple- \mathbf{q} states. We will determine the J - K phase diagram and calculate the temperature dependence of the order parameters. Details of the triple- \mathbf{q} orders will be also discussed.

A. Pseudospin-1/2 limit

In the limit of $E_1 \rightarrow \infty$, we can safely ignore the excited Γ_1 state for both the Hamiltonian (6) and the quadrupole operators $\mathbf{Q}(\mathbf{r})$. Thus $\mathbf{Q}(\mathbf{r})$'s are treated as pseudospin- $\frac{1}{2}$ operators, and the mean-field equation for the order parameter is easy to analyze [15]. For an isolated quadrupole, the response to the mean field \mathbf{h} has an

elementary form $\langle \mathbf{Q} \rangle = \mathcal{N}(h/T) \chi_0(T) \mathbf{h}$. Here, $\chi_0 = 1/T$ is the linear susceptibility, and the nonlinear correction is $\mathcal{N}(x) \equiv x^{-1} \tanh x$. The latter can be neglected for $|x| \ll 1$.

First, let us consider the region of ferro order ($2J < |K| < -2J$). The eigenmode analysis shows that the two eigenvalues of $\mathbf{J}(\mathbf{k})$ are degenerate, since the K terms vanish at $\mathbf{k}_0 = \mathbf{0}$. This means there is no preference for the ordering direction in the Q_u - Q_v quadrupole space. Recalling that each site has 12 nearest neighbors, one sets $\mathbf{h} = 12|J|\langle \mathbf{Q} \rangle$, and this leads to the condition of the transition temperature $12|J|\chi_0(T_c) = 1$. Its solution and the ground-state energy are

$$T_c = 12|J|, \quad E(T=0) = 6J, \quad (\text{FQ}). \quad (30)$$

For the antiferro case, one chooses one of the ordering vectors \mathbf{q}_* at the X points. Let us first discuss the O_{20} type realized for $K > 0$. See the eigenvector of the exchange coupling $\mathbf{J}(\mathbf{p})$ in Fig. 3. For the domain with $\mathbf{q}_* = \mathbf{k}_2 = (0, 2\pi, 0)$, the order parameter is $3y^2 - r^2$ type: $\mathbf{u}^\pm(\mathbf{k}_2)$ with $\bar{\vartheta}(\mathbf{k}_2) = \frac{4}{3}\pi$ or $\frac{1}{3}\pi$ as shown in Eq. (17). Since this ordering vector corresponds to two-sublattice (A and B) orders, one uses a two-sublattice version of the mean-field theory with $\mathbf{h}_{A,B} = -4J(\langle \mathbf{Q}_A \rangle + 2\langle \mathbf{Q}_B \rangle) \mp 4Kg(\delta_2)(\langle \mathbf{Q}_A \rangle - \langle \mathbf{Q}_B \rangle)$. Here, $-(+)$ is for $\mathbf{h}_{A(B)}$. The self-consistent equations for $\langle \mathbf{Q}_{A,B} \rangle$ lead to

$$T_c = 4J + 8K, \quad E(T=0) = -2J - 4K, \quad (\text{AFO}_{20}). \quad (31)$$

This antiferro quadrupole pattern is schematically shown in Fig. 7(a), where the quadrupole moments exhibit a ferro alignment on each zx plane, while an antiferro alignment along the y direction. Similarly, for $K < 0$, the antiferro O_{22} quadrupole solution leads to

$$T_c = 4J - 8K, \quad E(T=0) = -2J + 4K, \quad (\text{AFO}_{22}), \quad (32)$$

which are obtained from Eq. (31) by just replacing $K \rightarrow -K$. As an illustrative example, Fig. 7(b) shows the ordering pattern for O_{22} antiferro order with $\mathbf{q}_* = \mathbf{k}_3 = (0, 0, 2\pi)$, where the orbital type is $x^2 - y^2$: $\mathbf{v}^\pm(\mathbf{k}_3)$ with $\theta(\mathbf{k}_3) = \pm \frac{1}{2}\pi$. See also Fig. 3(b) and Eq. (17).

The ground state phase diagram determined from Eqs. (30)–(32) is shown in Fig. 8(a). The phase boundaries agree with those obtained by the mode analysis in Sec. II B. Note that the transition from the high-temperature disordered phase is always second order, while that between the different ordered states are first order as shown in Fig. 8(b).

B. Triple- \mathbf{q} orders

Now, let us consider realistic situations where $E_1 < \infty$, and examine whether the solutions in the previous section remain stable or not. The discussion above has examined only the leading instability due to the exchange

coupling $\mathbf{J}(\mathbf{p})$. A crucial point is missing, and that is the anisotropy in the Q_u - Q_v space that emerges from a hybridization of the excited Γ_1 state. When this anisotropy is taken into account, most parts of the ordered antiferro states in Fig. 8(b) are to be replaced by various triple- \mathbf{q} orders, and they have four-sublattice configurations in the real space. In this section, we concentrate on showing the results of the four-sublattice mean-field calculations. The mechanism stabilizing the triple- \mathbf{q} states will be discussed in detail in Sec. VI based on a phenomenological Landau theory.

For a general configuration of the four-sublattice order, the sublattice order parameters $\mathbf{Q}_{A,B,C,D}$ are related to those in the Brillouin zone at the four wavevectors \mathbf{k}_n ($n = 0, 1, 2, 3$). Labeling the sublattices as shown in Fig. 1(a), the relation is

$$\begin{bmatrix} \mathbf{Q}_A \\ \mathbf{Q}_B \\ \mathbf{Q}_C \\ \mathbf{Q}_D \end{bmatrix} = \frac{1}{2} \begin{bmatrix} 1 & 1 & 1 & 1 \\ 1 & 1 & -1 & -1 \\ 1 & -1 & -1 & 1 \\ 1 & -1 & 1 & -1 \end{bmatrix} \begin{bmatrix} \mathbf{Q}_{\mathbf{k}_0} \\ \mathbf{Q}_{\mathbf{k}_1} \\ \mathbf{Q}_{\mathbf{k}_2} \\ \mathbf{Q}_{\mathbf{k}_3} \end{bmatrix}, \quad (33)$$

where 1's in the matrix elements are 2×2 identity matrices. This is evident from the representation of the triple- \mathbf{q} states $\mathbf{Q}(\mathbf{r}) = \frac{1}{2} \sum_{n=0}^3 \cos(\mathbf{k}_n \cdot \mathbf{r}) \mathbf{Q}_{\mathbf{k}_n}$. We note that these order parameters $\mathbf{Q}_{\mathbf{k}_n}$ are real, since $-\mathbf{k}_n$ is equivalent to $+\mathbf{k}_n$ in the Brillouin zone.

For later purposes, we introduce the following polar coordinates of the quadrupole moments:

$$\begin{aligned} \mathbf{Q}_{\mathbf{k}_0} &\equiv Q \hat{e}_{\theta_\Gamma}, & \mathbf{Q}_{\mathbf{k}_1} &\equiv X \hat{e}_{\theta_X}, \\ \mathbf{Q}_{\mathbf{k}_2} &\equiv Y \hat{e}_{\theta_Y}, & \mathbf{Q}_{\mathbf{k}_3} &\equiv Z \hat{e}_{\theta_Z}. \end{aligned} \quad (34)$$

Here, $Q, X, Y, Z \geq 0$. We sometimes use an alternative notation

$$\mathbf{Q}_{\mathbf{k}_n} = X_n \hat{e}(\theta_n). \quad (35)$$

We will use these variables to distinguish and identify various states in the following sections.

V. MEAN-FIELD PHASE DIAGRAM

In this section, we will determine the phase diagram of the Γ_3 - Γ_1 model (10) based on a four-site mean-field approach. We will identify various ordered states and briefly summarize their transitions before more detailed analyses in the later sections.

First, we show the J - K phase diagrams for $T=0.5E_1$, $0.1E_1$, and 0 in the panels (a), (b), and (c), respectively, of Fig. 9. Each of the phases is identified, and its symmetry and schematic quadrupole configuration are summarized in Fig. 10. Simple antiferro (AFO_{22}) and ferro (FO_{20}) states appear in similar regions as those in Fig. 8(b), while the area of the AFO_{20} state is small at low temperatures. This is a striking difference from the results of the two-sublattice calculations. Note that

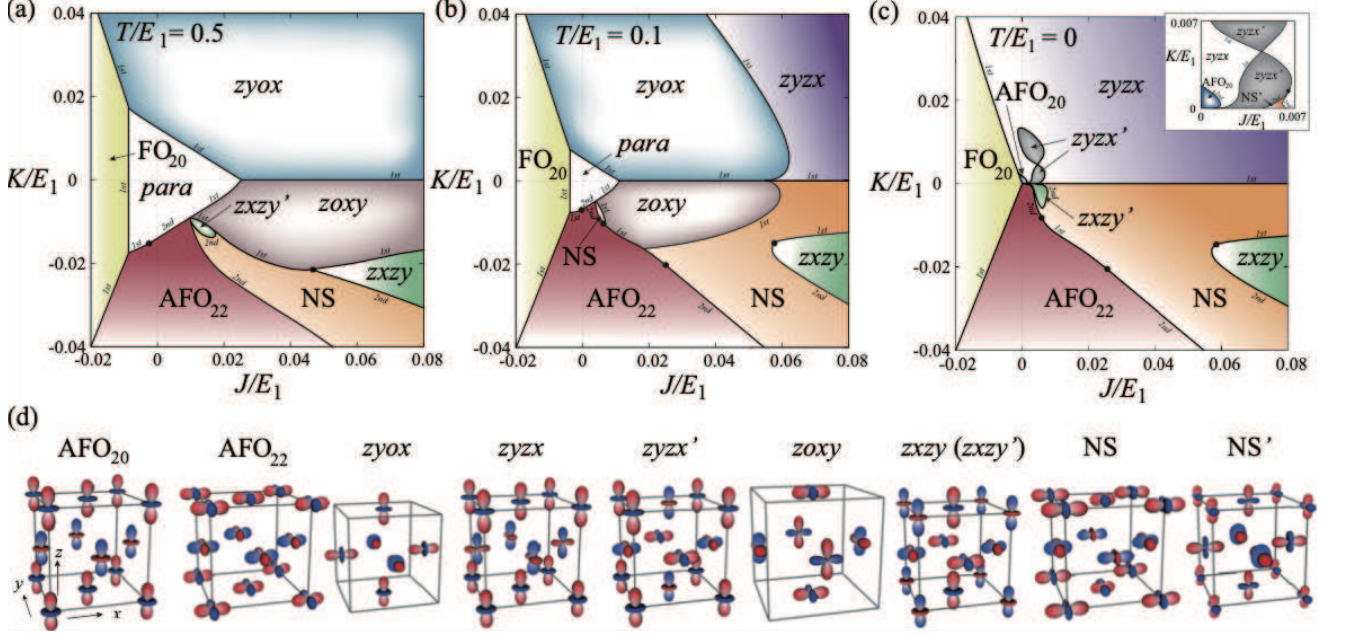


FIG. 9. (a)–(c) J - K phase diagram at fixed values of T , and (d) real-space configuration $\mathbf{Q}(\mathbf{r})$ in each ordered state. (a) $T/E_1 = 0.5$, (b) 0.1 , and (c) 0.0 . The order of transition is indicated for the borders in (a)–(c) as “1st” or “2nd”. Tricritical points are marked by filled circles. “para” in (a) and (b) denotes a disordered phase with no symmetry breaking. See also Fig. 10 for the symmetry and \mathbf{Q} configuration in each state. In (b), a region of the $zxzy$ state exists near $(J, K)/E_1 \sim (0.005, -0.006)$, but it is too small to see. In (c), the $zxzy'$ state contains a small $zxzy$ region but they are not distinguished since both have the same symmetry. Inset in (c) is a zoom up of the part near the origin for $K > 0$. The $zyxz'$ state has two disconnected parts. In the part at large J , two of the four sublattice \mathbf{Q} 's are the largest there (see the $zyxz'$ state in Fig. 10). In the part at small J , one \mathbf{Q} is larger than the others, (see the $zyxz$ state in the Fig. 10). A small region of the NS' state [not shown in the main panel of (c)] bridges the $zyxz'$ and $zyxz$ states via two second-order transitions. The phase diagram at $K = 0$ is discussed in Appendix D. (d) Schematic quadrupole configuration in each ordered state in a cubic unit cell. In the $zyxz$ state, moments at the corners have a slightly different magnitude from those at the face centers.

the ferro quadrupole state is named FO_{20} rather than FQ , since the system favors O_{20} over O_{22} due to the anisotropy driven by the hybridization α of the excited Γ_1 state in Eq. (5). Other regions in the J - K parameter space are occupied by various types of the triple- \mathbf{q} orders or otherwise the high-temperature disordered state denoted by *para*. We name these triple- \mathbf{q} states by a combination of four letters according to the real-space quadrupole configurations in the four sublattices [15]. These four letters denote the principle axis of uniaxial orders in the sublattices A–D. For example, *zyox* means that \mathbf{Q}_A , \mathbf{Q}_B , and \mathbf{Q}_D are z^2 , y^2 , and x^2 type, respectively. The C-sublattice is disordered, namely, “o” represents disordered. Thus the *zyox* and *zoxy* states are partially ordered. They appear only at high temperatures and do not exist in the ground state phase diagram in Fig. 9(c). In these partial-order states, the ferro component has zero amplitude, $Q = 0$, while $Q \neq 0$ in the fully ordered states. The phase with the lowest symmetry in the four-site mean-field calculations is named *no symmetry state* (NS and NS'). They are not invariant

for any operation of the cubic lattice symmetry or for sublattice exchanges.

We comment about new aspects of the phase diagrams untouched in the first report [15]. The first aspect is about the NS' state. This appears when $K > 0$ in an extremely small region near the phase boundary between the $zyxz'$ and $zyxz$ states at very low temperatures as shown in the inset of Fig. 9(c). As shown in Fig. 10, the two states $zyxz$ and $zyxz'$ have the same symmetry, and thus the transition between the two should be first order. When the NS' state intervenes into their boundary, the new boundary becomes a line of second-order transition with either the $zyxz$ or $zyxz'$ state. Remember that the two modes \mathbf{Q}_{k_1} and \mathbf{Q}_{k_2} are both dominant in the $zyxz'$ state (i.e., $X = Y > Z$), while only one mode is dominant in the $zyxz$ state: \mathbf{Q}_{k_1} ($X > Y = Z$). See Fig. 10. Thus, as J increases starting from the $zyxz'$ state, we observe that the balance of the two modes is eventually lost such that $X > Y$ in the NS' state and then Y approaches Z with approaching the $zyxz$ state. This change may happen continuously, and this explains

	C_4	C_3	σ_d	σ_h	induced FQ	$\mathbf{Q}(\mathbf{r})$	$\mathbf{Q}_{\mathbf{k}_n}$
<i>para</i>					—		
FO ₂₀		×			—		
AFO ₂₀		×			Yes		
AFO ₂₂	×	×	×		Yes		
<i>zyox</i>					No		
<i>zyzx</i>		×			Yes		
<i>zyzx'</i>		×			Yes		
NS'	×	×	×		Yes		
<i>zoxxy</i>	×		×		No		
<i>zxzy</i>		×			Yes		
<i>zxzy'</i>		×			Yes		
NS	×	×	×		Yes		

FIG. 10. Symmetry of the ordered states and schematic quadrupole configurations in real space $\mathbf{Q}(\mathbf{r})$ and in momentum space $\mathbf{Q}_{\mathbf{k}_n}$ ($n = 0, 1, 2, 3$). The first four columns show a list of broken symmetries among those of the original point group: (C_4) the four-fold rotation about a principal axis, (C_3) the three-fold rotation about $[111]$ direction, (σ_d) the mirror with respect to $(1\bar{1}0)$ plane, (σ_h) the mirror with respect to (001) plane. Broken ones are indicated by a \times symbol. \mathbf{Q} 's are shown by arrows in the two-dimensional quadrupole space where the horizontal (vertical) direction corresponds to the Q_u (Q_v) component. The *zyzx* (*zxzy*) and *zyzx'* (*zxzy'*) states have the same symmetry, but are distinguished by the direction of the smallest $\mathbf{Q}(\mathbf{r})$ ($\mathbf{Q}_{\mathbf{k}_0}$). Circles with dots are guide for the eye. $\mathbf{Q}(\mathbf{r})$'s are calculated using Eq. (33) from $\mathbf{Q}_{\mathbf{k}_n}$'s, for the domain chosen in Figs. 11–13.

the calculated results. We note that while the NS and NS' states have the same symmetries, they are distinct. Further details are analyzed in Appendix D.

The second new aspect is about a tiny region of the *zxzy'* state near the small island of the NS state at $T/E_1 = 0.1$ in Fig. 9(b). The area of this is too small to see there. The third aspect is about the order of transitions. Some parts of the phase boundaries are of the first-order transition, and they are separated from the parts of second order transition by tricritical points. In Ref. [15], these tricritical points are shown only in the ground state phase diagram corresponding to Fig. 9(c). We have carefully examined the order of transitions at finite temperatures, and the locations of the tricritical

points are indicated by filled circles also in the panels (a) and (b). For example, a tricritical point exists on the *para*-AFO₂₂ phase boundary. This was one of our predictions in Ref. [11], where antiferro orders only differentiate two sublattices inside the unit cell without breaking the translation symmetry. The discussion there is applicable to the present case that an instability of $\mathbf{Q}_{\mathbf{k}}$ takes place at the X points in the Brillouin zone.

Let us now examine the temperature dependence of the order parameters. Figure 11 shows their amplitudes $|\mathbf{Q}_{\mathbf{k}_\ell}|(T)$ for the typical ordered states. We just show the results for one of the degenerate domains. The transitions of the *para*-FO₂₀ (a), *para*-*zyox* (b), AFO₂₀-*zyox* (b), and NS-*zoxxy* (f) are clearly all discontinuous, i.e. first order. The transitions of the *zyox*-*zyzx* (*zyzx'*) [(c) and (d)] and *para*-*zoxxy* [(f)–(h)] are either first order or continuous as depending on the parameters. In contrast, the transitions of the *para*-AFO₂₂ [(g)], NS-AFO₂₂ [(e)], and NS-*zxzy* [(g)] are all continuous for the parameter sets used. We note that there is no direct *para*-AFO₂₀ transition. The high-temperature side above the AFO₂₀ state is always the *zyox* state.

Next, we discuss the order parameter variations in the J - K space for several fixed values of T . To this end, we parametrize J and K as

$$(J, K) \equiv \bar{J}(\cos \xi, \sin \xi), \quad (36)$$

and vary ξ from 0 to 2π . Figure 12 shows the ξ -dependence of $|\mathbf{Q}_{\mathbf{k}_\ell}|$ for $\bar{J}=0.08E_1$ at $T=E_1$ and $0.1E_1$. In addition to $|\mathbf{Q}_{\mathbf{k}_\ell}|$'s, we introduce

$$Q_{XYZ} \equiv X + Y + Z, \quad (37a)$$

$$Q_{E_g,1} \equiv \frac{1}{\sqrt{6}}(2Z - X - Y), \quad Q_{E_g,2} \equiv \frac{1}{\sqrt{2}}(X - Y), \quad (37b)$$

with

$$Q_{E_g} \equiv (Q_{E_g,1}^2 + Q_{E_g,2}^2)^{1/2} \\ = [X^2 + Y^2 + Z^2 - \frac{1}{3}(X + Y + Z)^2]^{1/2}. \quad (37c)$$

These $Q_{E_g,1}$ and $Q_{E_g,2}$ describe the symmetry breaking in the triple- \mathbf{q} states. For example, both of the *zoxxy* and *zyox* partial ordered states have $X=Y=Z$, and thus $Q_{E_g} = 0$. These two differ in the angle variables $\theta_{X,Y,Z}$. The transition between AFO₂₂ and NS states is about the changes in the two modes (X and Y in Fig. 12). They stay zero inside the AFO₂₂ state and emerge continuously in the NS state. The two states have the same internal symmetries in Fig. 10, and what breaks is the translation symmetry; A two-sublattice order changes to a four-sublattice one. At the NS-*zxzy* transition, the equality of the largest amplitude modes breaks. Namely, the equality $Z = X$ in the *zxzy* state breaks down in the NS state. The related transition is either first order or continuous as shown in Figs. 9 and 12.

Let us switch to the analysis of the moment directions. In the relatively high symmetry states, AFO₂₀, AFO₂₂,

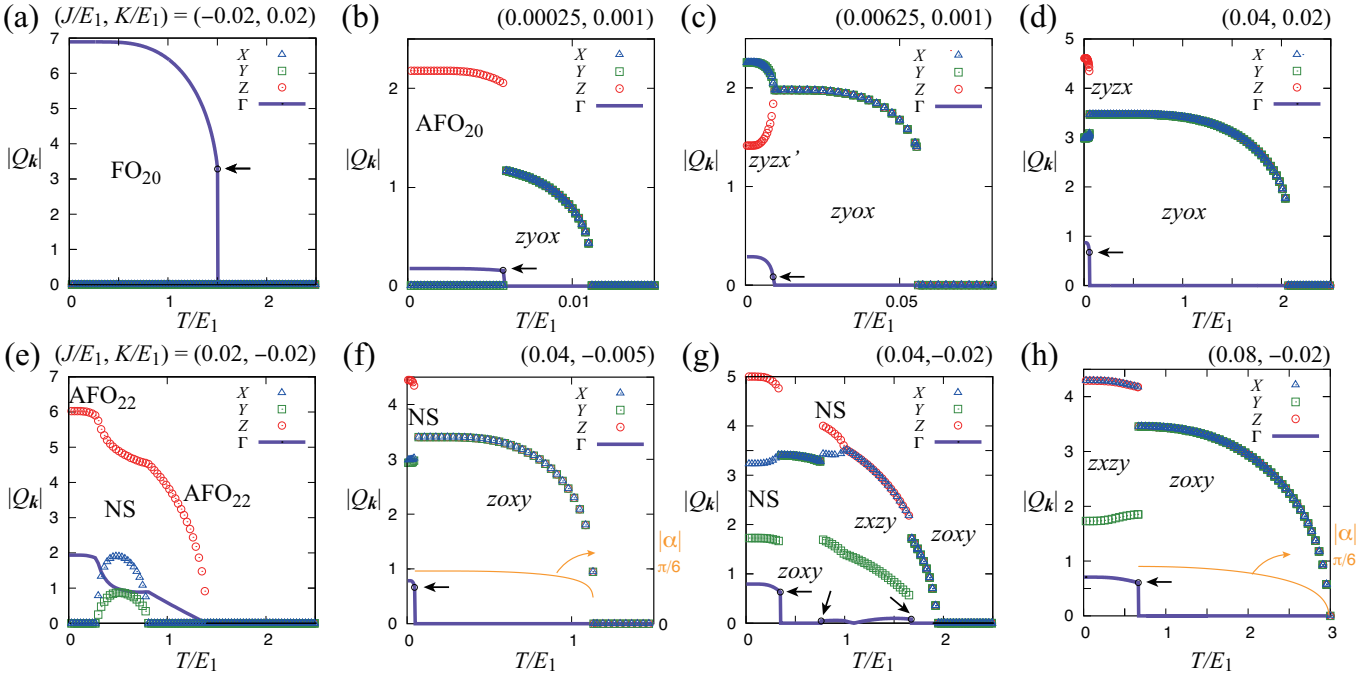


FIG. 11. Temperature dependence of the moment magnitudes $|Q_{k_n}|$ for (a)–(d) $K > 0$ and for (e)–(h) $K < 0$. Blue Δ , green \square , red \circ , and purple line show $|Q_{k_1}| = X$, $|Q_{k_2}| = Y$, $|Q_{k_3}| = Z$, $|Q_{k_0}| = \Gamma = Q$, respectively. The parameter set $(J, K)/E_1$ is shown in each panel. Discontinuous changes in $\Gamma = Q$ are marked by a black arrow. In (f) and (h) also plotted is $\alpha \equiv (\theta_X + \theta_Y + \theta_Z)/3 - \pi/2 \pmod{2\pi}$. In (b)–(d) and (f), the transition between the para and $zyox$ or $zoxy$ states is discontinuous.

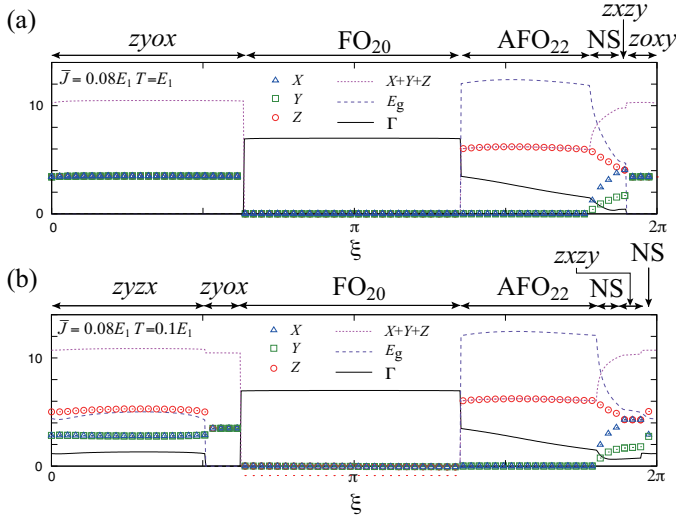


FIG. 12. ξ dependence of $|Q_{k_n}|$. X , Y , Z , and Γ are those defined in Fig. 11. Dotted and dashed lines represent Q_{XYZ} and Q_{Eg} , respectively. $\bar{J}/E_1 = 0.08$. (a) $T/E_1 = 1.0$ and (b) 0.10 .

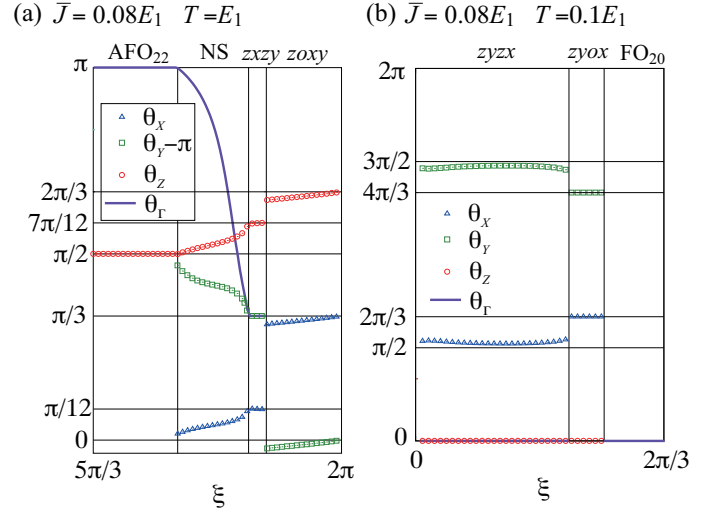


FIG. 13. Order parameter directions $\theta_{X,Y,Z,\Gamma}$ in a specific domain at high and low temperatures for $\bar{J}/E_1 = 0.08$. Note that θ is not shown when its $Q_{k_n} = 0$, e.g., θ_Γ for the $zoxy$ and $zyox$ states.

and $zyox$, the directions $\theta_{\Gamma,X,Y,Z}$ are fixed to the high symmetry axes $\frac{1}{4}\omega \times (\text{integer})$. Figure 13 shows typical examples of their change as a function of ξ . In Fig. 13(a), θ_X and θ_Y seem to abruptly appear at the AFO₂₂-NS

phase boundary. However, it does not mean that the transition is of first order, since $X = Y = 0$ inside the AFO₂₂ state. In the partially ordered $zoxy$ state, the quadrupole directions are equally separated and satisfy the relations $\theta_Y - \theta_X = \theta_X - \theta_Z = \theta_Z - \theta_Y = \omega$, by properly

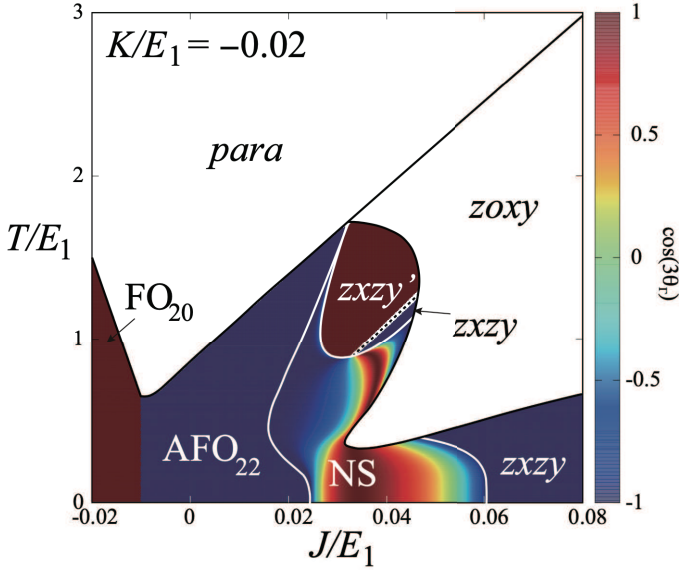


FIG. 14. Color plot of $\cos(3\theta_\Gamma)$ in the J - T plane for $K/E_1 = -0.02$. Phase boundaries are indicated by black or white lines. $\theta_\Gamma = \omega \times (\text{integer})$ for the FO_{20} and zxzy' states, while $\theta_\Gamma = \pi + \omega \times (\text{integer})$ for the AFO_{22} and zxzy states. Note that Q stays zero in the zoxy state. A dotted line represents the boundary between the zxzy and zxzy' states, but this does not mean a phase transition there. This is just the line of $Q = 0$.

shifting the origin of the four-site unit cell, since this shift changes two of the three directions by the angle π . See Eq. (33). In contrast, the angle average $\alpha \equiv (\theta_X + \theta_Y + \theta_Z)/3$ varies continuously inside the zoxy state as shown in Figs. 11(f), 11(h), and 13(a). Note that the sign of α distinguishes the two domains. The counterpart of this state is zyox in the $K > 0$ region. There, α is fixed to 0 and $\theta_Z - \theta_Y = -\omega$, while the other θ -relations are unchanged. See Fig. 13(b). One should also note that these zyox and zoxy states have no uniform moment and thus $Q = 0$.

While the direction of the uniform moment θ_Γ changes continuously in the NS state, it is fixed in the other states to one of the symmetry axes $\frac{1}{2}\omega \times (\text{integer})$. Figure 14 plots $\cos(3\theta_\Gamma)$ in the J - T plane for $K/E_1 = -0.02$. Inside the NS state, it varies continuously between -1 and 1 . One should also note that the para - zoxy phase boundary extends smoothly across the multi-critical point at $J/E_1 \sim 0.03$ to the para - AFO_{22} boundary. We will discuss this aspect in Sec. VIII A.

We close this section by discussing the consequence of the topological transition explained in Sec. III. In the following discussion, we discuss the local quadrupole moments Q_{A-D} . In the mean field theory, strong interactions J and K enhance the effective mean fields. Thus, the local moments increase their amplitude correspondingly for most of the cases. However, when Q points to one of the special directions $\theta = n\omega + \pi$ (n : integer), its

amplitude is pinned to $|Q| = 1$ and does not grow even when the interactions increase. This is because the system belongs to the region of “half-integer spin” where $|\langle Q \rangle_0(\Phi = n\omega + \pi)| = 1$ as shown in Fig. 5, as far as the mean fields are not so strong ($\Theta < \Theta_c$). With further increasing the interactions, the parameter Θ increases and finally reaches $\Theta = \Theta_c$, where the topological transition occurs. For larger interactions exceeding the critical value ($\Theta > \Theta_c$), the ground state wavefunction is “integer spin” type, and $|Q|$ is no longer pinned and grows continuously as shown in Fig. 6. The point is that as long as the local mean-field direction is $\Phi = n\omega + \pi$, $|Q|$ cannot change up to $\Theta = \Theta_c$. Once the direction Φ tilts from $n\omega + \pi$, the quadrupole moments also tilt and their amplitude can change.

Such a Q pinning is indeed realized in the zyzx' , zxzy' , and AFO_{20} states. Figure 15(a) is a color plot of the minimum amplitude $Q_{\min} \equiv \min |Q_{A,B,C,D}|$ for $T = 0$. It clearly shows that $Q_{\min} = 1$ in the zyzx' , zxzy' , and AFO_{20} states. Apart from these three states, there is a regime with $Q_{\min} \simeq 1$ inside the NS state for $K/E_1 \sim -0.01$ and $J/E_1 \sim 0.01$. In the NS state, the quadrupole moment changes its direction away from $\theta = n\omega + \pi$, and Q_{\min} varies continuously. In the zyzx state for $K > 0$, no moments point to $\theta = n\omega + \pi$, and thus no such pinning effect takes place. In contrast, in the zxzy state for strong coupling J and $K < 0$, one moment points to $\theta = n\omega + \pi$, but this time the system is already in the “integer-spin” domain, and thus pinning effects are absent.

Figures 15(b) and 15(c) illustrate the variation of the sublattice moments Q_{A-D} with increasing J at $T = 0$. The panel (b) is the data for $K/E_1 = 3.9 \times 10^{-3}$ and shows that Q_A stays $(-1, 0)^T$ inside the zyzx' state and jumps to $(1, 0)^T$ at the transition to the zyzx state. The panel (c) is for $K/E_1 = -3.9 \times 10^{-3}$ and shows that $|Q_A| = 1$ inside the zxzy state and the transition to the NS state is continuous. This is a clear contrast to the cases for $K > 0$, and the direction of Q_A gradually changes around the transitions. These transitions occur inside the regime where the A-sublattice state behaves as a “half-integer spin”. We also point out that the variations of Q_{A-D} in the panel (c) is quite complicated.

VI. LANDAU THEORY

In this section, we employ a phenomenological Landau analysis and interpret the determined mean-field phase diagrams (Fig. 9). Our aim is to explain the stability of various ordered states and describe their transitions based on a phenomenological theory.

The determined phase diagrams in Sec. V are quite complicated, and their complete analysis is beyond the scope of the present paper. Since the partially ordered zyox and zoxy states are exotic states characteristic to the present model, we set them as our main targets and investigate mainly their stability mechanism and insta-

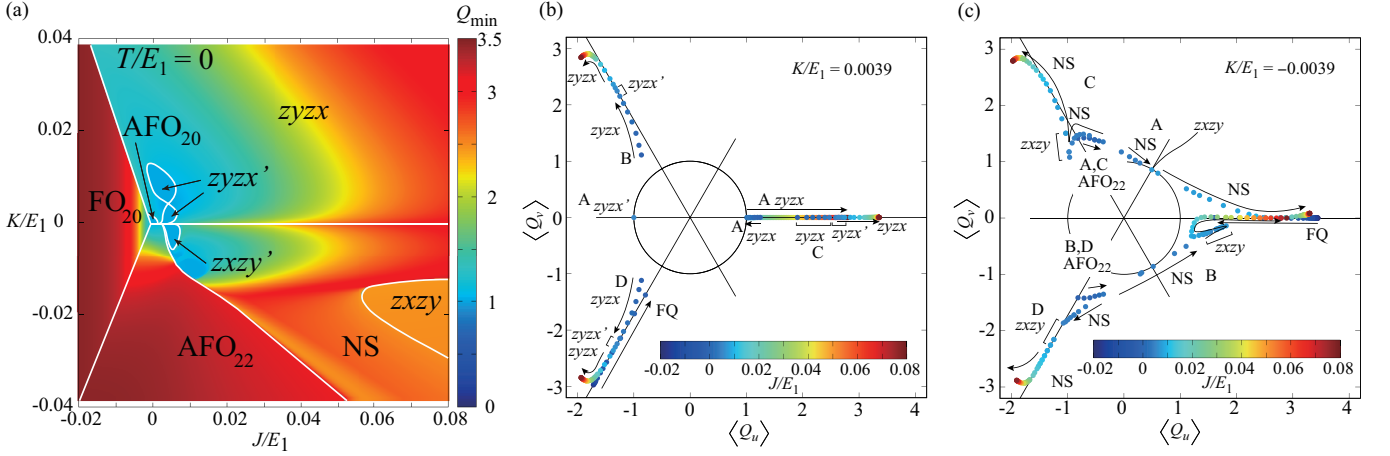


FIG. 15. (a) Color plot of Q_{\min} in the J - K plane for $T = 0$. (b) Trajectories of the sublattice moments Q_A - Q_D as J varies at $K/E_1 = 3.9 \times 10^{-3}$ and $T = 0$ fixed. (c) Trajectories now for $K/E_1 = -3.9 \times 10^{-3}$. Arrows indicate the variation upon increasing J and the symbol color represents J -value. Unit circles and lines indicating directions of $\theta = \omega \times (\text{integer})$ are guides for the eye.

bility to other states.

In our phenomenological analysis, we will construct the Landau free energy in terms of $Q_{\mathbf{k}_0}$ and $Q_{\mathbf{k}_\ell}$'s and analyze various triple- \mathbf{q} orders in detail. An important point is that the ordering vectors $\mathbf{q}_* = \mathbf{k}_\ell$ allow cubic couplings of the three antiferro modes $Q_{\mathbf{k}_\ell}$, which play a crucial role in stabilizing several ordered states in this system. This analysis succeeds in explaining most of the results of the microscopic mean field calculations in Sec. IV.

A. Landau-Ginzburg free energy expansion

Let us first introduce the local free energy $f_{\text{loc}}(\mathbf{r})$ with the quadrupole moment $\phi(\mathbf{r}) \equiv [(\phi_u, \phi_v)(\mathbf{r})]^T$ as

$$f_{\text{loc}}(\mathbf{r}) = \frac{1}{2}a_0(T)|\phi(\mathbf{r})|^2 - b[\phi_u^3(\mathbf{r}) - 3\phi_u(\mathbf{r})\phi_v^2(\mathbf{r})] + c|\phi(\mathbf{r})|^4 + O(|\phi(\mathbf{r})|^5). \quad (38)$$

The coefficients a_0 , b , and c are all positive constants depending on temperature, which may be derived from the local CEF model through a Legendre transformation [11]. It is customary to consider the temperature dependence of $a_0(T)$ alone and neglect the changes in b and c . One should note that $a_0(T)$ is the inverse of local quadrupole susceptibility and decreases monotonically towards zero with decreasing temperature. An important characteristic of this system is the presence of the b -term. This third-order term exists only for order parameters with even parity under both time reversal and space inversion operations, and our quadrupole moments belong to this category. Its explicit form in terms of ϕ_u and ϕ_v is independent of the details of the system, and determined from the coefficient related to the reduction of the triple product of the Γ_3 representation to the trivial one, $\Gamma_3 \otimes \Gamma_3 \otimes \Gamma_3 \rightarrow \Gamma_1$.

Following the conventional procedure, we add to Eq. (38) the exchange interaction energy, which are given by the mean-field approximation. Thus the total free energy density $\bar{f} = F/N$ reads as

$$\bar{f} \equiv \frac{1}{N} \sum_{\mathbf{r}} \left[f_{\text{loc}}(\mathbf{r}) + \sum_{j=1}^6 \phi(\mathbf{r} + \delta_j) \cdot \mathbf{J}_{\delta_j} \phi(\mathbf{r}) \right] \quad (39a)$$

$$= \frac{1}{N} \sum_{\mathbf{p}} \phi(-\mathbf{p}) \cdot \left[\frac{1}{2}a_0 + \mathbf{J}(\mathbf{p}) \right] \phi(\mathbf{p}) - \frac{b}{N^{3/2}} \sum' \phi_u(\mathbf{p}_3) [\phi_u(\mathbf{p}_1)\phi_u(\mathbf{p}_2) - 3\phi_v(\mathbf{p}_1)\phi_v(\mathbf{p}_2)] + \frac{c}{N^2} \sum' [\phi(\mathbf{p}_1) \cdot \phi(\mathbf{p}_2)] [\phi(\mathbf{p}_3) \cdot \phi(\mathbf{p}_4)], \quad (39b)$$

where \sum' denotes the sum over \mathbf{p}_i 's under the constraint $\sum_i \mathbf{p}_i = (\text{some reciprocal lattice vector } \mathbf{G})$. The interaction matrix \mathbf{J}_{δ} is given by Eq. (7), while its Fourier transform $\mathbf{J}(\mathbf{p})$ is given by Eq. (11b). We have neglected a constant energy, and N is the number of the sites. The terms for $\mathbf{G} \neq \mathbf{0}$ are Umklapp processes, and they will turn out to be important later.

Since our main concern is various antiferro orders of quadrupole, we split the total free energy as follows:

$$\bar{f} = f_X + f_\Gamma + f_{\Gamma X} + f_{\text{other}}, \quad (40)$$

where f_X is the antiferro part, i.e., contributions of $\phi(\mathbf{k}_\ell)$'s alone. f_Γ is the ferro part contributed by $\phi(\mathbf{k}_0)$, and $f_{\Gamma X}$ is the coupling of $\phi(\mathbf{k}_\ell)$'s with $\phi(\mathbf{k}_0)$. We will show that this coupling modifies and eventually destabilizes several antiferro orders. Lastly, f_{other} is the sum of all the remaining parts.

Figure 16 summarizes the relations among various states in the J - K plane along with the section numbers where they are discussed. The detailed discussions about several states are summarized in Appendices. In particular, the configurations at $K = 0$ are discussed in detail in

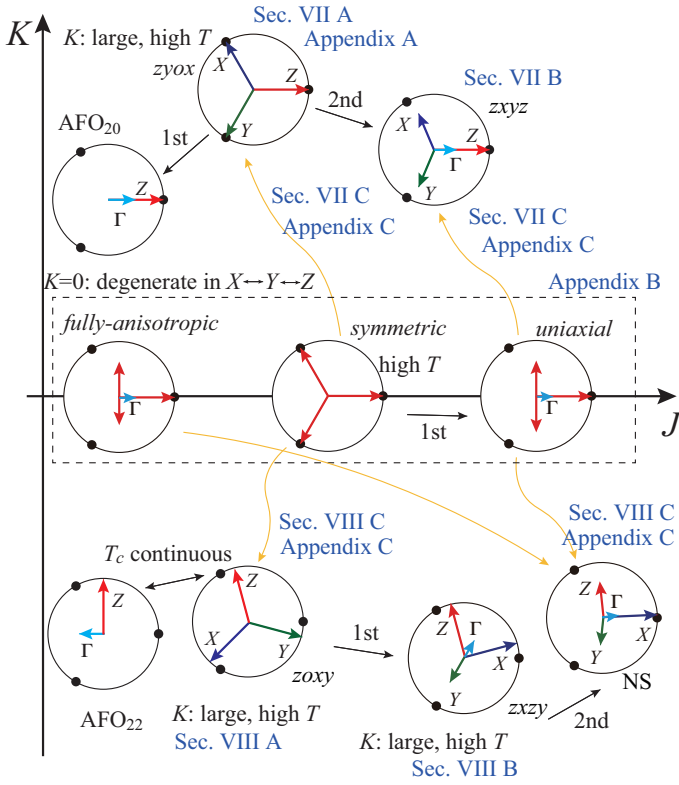


FIG. 16. Summary of the order parameter configurations discussed on the basis of Landau theory in Secs. VI–VIII. We list only the major states (NS' not included) and also indicate in which section each state is discussed. The three configurations enclosed by a dashed rectangular are those for $K = 0$. They are analyzed in Appendix B. The label “1st” or “2nd” marked for an arrow indicates the order of the corresponding transition, but one should note that the possibility of a first order transition is not excluded for any of them. Yellow arrows indicate how each configuration at $K \neq 0$ evolves from one of the degenerate configurations at $K = 0$.

Appendix B. The yellow arrows illustrate schematically the relations between the states at $K \neq 0$ and those at $K = 0$ through small K perturbations.

B. Free energy of the antiferro modes

In this section, we will rewrite the antiferro part f_X into a convenient form for later analyses. When $|K| + 2J > 0$, the maximally negative eigenvalue of the matrix $J(\mathbf{p})$ is $\Lambda_{\min} = -2J - 4|K|$ and it is realized at $\mathbf{p} = \mathbf{k}_\ell$'s. Thus it is natural to expect a single- \mathbf{q} order with the ordering vector located at one of \mathbf{k}_ℓ 's. The transition temperature of this order $T = T_c^0$ is determined by the equation $\frac{1}{2}a_0(T_c^0) + \Lambda_{\min} = 0$. However, the situation is not so simple in this system, since the free energy contains the third-order terms including $\phi(\mathbf{k}_\ell)$'s. The three wavevectors at the X points satisfy the relation

$\mathbf{k}_1 + \mathbf{k}_2 + \mathbf{k}_3 = (2\pi, 2\pi, 2\pi) = \mathbf{G}$, and thus the corresponding third-order coupling is nonvanishing. This may lead to a first-order transition to a triple- \mathbf{q} state with a transition temperature $T_c > T_c^0$.

To analyze such triple- \mathbf{q} states, we restrict the degrees of freedom to those $\{\phi(\mathbf{k}_\ell)\}_{\ell=1,2,3}$ and ignore other modes. Notice that $\phi(\mathbf{k}_\ell)$'s are real, since each \mathbf{k}_ℓ is equivalent to $-\mathbf{k}_\ell$, and proportional to \sqrt{N} in the antiferro ordered states. We thus rescale them as $\psi^{(\ell)} \equiv \phi(\mathbf{k}_\ell)/\sqrt{N}$. The related part of the free energy density reads as

$$f_X = \sum_{\ell} \psi^{(\ell)} \cdot \left[\frac{1}{2}a_0(T) + J(\mathbf{k}_\ell) \right] \psi^{(\ell)} - 6b \left[\psi_u^{(1)} \psi_u^{(2)} \psi_u^{(3)} - \sum_{\ell} \psi_u^{(\ell)} \psi_v^{(\ell+1)} \psi_v^{(\ell+2)} \right] + c \sum_{\ell} |\psi^{(\ell)}|^4 + 2c' \sum_{\ell < \ell'} |\psi^{(\ell)}|^2 |\psi^{(\ell')}|^2 + 4c'' \sum_{\ell < \ell'} [\psi^{(\ell)} \cdot \psi^{(\ell')}]^2, \quad (41)$$

where one should understand that $\psi^{(\ell+3)} \equiv \psi^{(\ell)}$. Here, although the direct calculations provide $c' = c'' = c$, we regard these three as independent parameters, since each term is separately invariant. We rewrite Eq. (41) in terms of the polar coordinates defined as $\psi^{(\ell)} = (\psi_u^{(\ell)}, \psi_v^{(\ell)})^T \equiv X_\ell \hat{e}(\theta_\ell)$ as in Eqs. (34) and (35). We also define $\mathbf{X} \equiv (X_1, X_2, X_3)$ and $\boldsymbol{\theta} \equiv (\theta_1, \theta_2, \theta_3)$ for later use. Substituting these into Eq. (41), we obtain

$$f_X = \left[\frac{1}{2}a_0(T) - 2J \right] R^2 + cR^4 - 4K \sum_{\ell} X_\ell^2 \cos(2\theta_\ell + \ell\omega) - 6bX_1X_2X_3 \cos \bar{\theta} + 2(c' - c) \sum_{\ell < \ell'} X_\ell^2 X_{\ell'}^2 + 4c'' \sum_{\ell < \ell'} X_\ell^2 X_{\ell'}^2 \cos^2(\theta_\ell - \theta_{\ell'}), \quad (42)$$

where

$$R^2 \equiv X_1^2 + X_2^2 + X_3^2, \quad \bar{\theta} \equiv \theta_1 + \theta_2 + \theta_3. \quad (43)$$

Further analysis depends on the sign of the anisotropic interaction K . In the following sections, we will discuss the two cases separately.

VII. ANALYSIS OF THE $K > 0$ PART

In this section, we perform phenomenological analyses on the triple- \mathbf{q} states for the $K > 0$ part of the mean-field phase diagrams. We will mainly examine two limiting cases, large and small K limits, in the following sections. We first attempt to find solutions that minimize f_X in Eq. (42) for the case of $K > 0$. As discussed in Sec. II B, the eigenvector of the maximally negative eigenvalue of $J(\mathbf{k}_\ell)$: $\Lambda_{\min} = \Lambda_-(\mathbf{k}_\ell)$ corresponds to $\boldsymbol{\theta} = (\omega, -\omega, 0)$. We will fix these angles and find an approximate solution in Sec. VII A. Then, we will introduce their couplings to the uniform moment in Sec. VII B. This mode coupling

induces a finite uniform moment and also deforms the angles θ from $(\omega, -\omega, 0)$. In Sec. VII C, we will discuss possible triple- \mathbf{q} states in the small K limit, starting from the results for $K = 0$.

A. Large K case: the $zyox$ state

In the limit of $K \rightarrow \infty$, the free energy f_X has a symmetry inherited from the K -term. The replacement $\theta_\ell \rightarrow \theta_\ell + \pi$ for any ℓ does not change the K -term, and this results in an eightfold degeneracy of f_X minimum: $\theta = (\omega, -\omega, 0) + (n_1, n_2, n_3)\pi$ where $n_j = 0, 1$. The third-order term favors four out of these eight possibilities. Since $b > 0$, the favored ones are those with $\sum_j n_j = (\text{even})$.

We continue the minimization procedure for f_X now with respect to X_ℓ 's. This is a cumbersome but straightforward calculation, and we show only its results. There exist two types of solutions, and both are controlled by the renormalized second-order coupling

$$a_X(T) \equiv \frac{1}{2}a_0(T) - 2J - 4K. \quad (44)$$

One type is the solution that only one of X_ℓ 's is non-vanishing, while $X_1 = X_2 = X_3$ in the other type. The former one is the single- \mathbf{q} order, and the latter one is the $zyox$ order.

A solution for the single- \mathbf{q} order ($X_\ell = \delta_{\ell 3} R_{1\mathbf{q}}^*$) exists when $a_X(T) < 0$, and it is represented as follows

$$R_{1\mathbf{q}}^* \equiv \left[\frac{-a_X(T)}{2c} \right]^{1/2}, \quad f_X^{1\mathbf{q}} = -\frac{a_X(T)^2}{4c}. \quad (45)$$

See Eq. (A9) in Appendix A.

A $zyox$ -type solution ($X_1 = X_2 = X_3 =: R_{zyox}^*/\sqrt{3}$) appears as a local minimum, and we denote its transition temperature by T^* . See Eq. (A10) for the effective free energy as a function of R_{zyox}^* . We define R^* as the R_{zyox}^* value just below T^* . These values are determined as

$$R^* \equiv \frac{\sqrt{3}b}{4(c+c_1/3)}, \quad a_X(T^*) = \frac{\sqrt{3}}{2}bR^* \equiv a^* > 0, \quad (46)$$

where

$$c_1 \equiv 2(c' - c) + c''. \quad (47)$$

Then, the temperature dependence of important quantities is written as

$$R_{zyox}^* = R^* [1 + \sqrt{1 - a_X(T)/a^*}], \quad (48)$$

$$f_X^{zyox} = (4\sqrt{3})^{-1}bR^{*3} \mathcal{F}_2(1 - a_X(T)/a^*), \quad (49)$$

where $\mathcal{F}_2(x) = 4 - 3(1+x)^2 - 8x^{3/2}$.

Let us now compare the stability of these two ordered states by calculating their free energies. One should recall

that $a_X(T)$ decreases monotonically with lowering temperature. Four temperatures characterize possible phase transitions:

$$T^\times < T_{1\mathbf{q}}^c < T_{zyox}^c < T^*. \quad (50)$$

As defined before, T^* is the temperature where a solution of the $zyox$ order appears. However, since its free energy is still higher than that for the disordered phase, this order is not realized yet. The $zyox$ order is stable below T_{zyox}^c and this temperature is determined by the condition $a_X(T_{zyox}^c) = \frac{8}{9}a^*$. With further lowering temperature, the effective second-order coupling $a_X(T)$ vanishes eventually and this defines the “transition temperature” of the single- \mathbf{q} order $T_{1\mathbf{q}}^c$. Below this temperature, the single- \mathbf{q} ordered state is more stable than the disordered state. However, its free energy $f_X^{1\mathbf{q}}$ remains higher than f_X^{zyox} for a while, and thus the single- \mathbf{q} order does not appear yet. With further decreasing temperature, $f_X^{zyox}(T)$ may cross with $f_X^{1\mathbf{q}}(T)$. This determines the final characteristic temperature T^\times , below which the single- \mathbf{q} order is finally realized. Equating the two free energies, T^\times is obtained as a solution of the following equation

$$\frac{c_1}{8c} = x^{-2} \left[1 - \frac{3}{2}x + (1-x)^{3/2} \right] \Big|_{x=a(T^\times)/a^*}. \quad (51)$$

One should note that the transitions at T_{zyox}^c and T^\times are both first order.

We have not examined a possibility of double- \mathbf{q} orders, and there is a reason for that. In the free energy density f_X in Eq. (42), the third-order term generally has a nonzero coupling $b \neq 0$. Thus, when two order parameters are nonvanishing, say $X_1, X_2 > 0$, their product acts as a field linearly coupled to X_3 , and this induces a nonvanishing amplitude of X_3 . Therefore, any double- \mathbf{q} order is inevitably converted to a triple- \mathbf{q} order, and genuine double- \mathbf{q} orders do not exist as a stable phase.

Unfortunately, the above free energy analysis does not fully explain the actual phase diagram in the $K > 0$ part. For example, the $zyzx$ state is hardly realized. This is because we have not taken account of coupling to the uniform component $\psi_0 \equiv \phi(\mathbf{k}_0)/\sqrt{N}$, or its effects on tilting θ from the assumed values. In addition, the single- \mathbf{q} state also couples with ψ_0 and this lowers the free energy. Thus, the above analysis is satisfactory only for the $zyox$ state, and we need to include those corrections for the $zyzx$ and single- \mathbf{q} states. Nonetheless, it remains true that the $zyox$ state appears at a temperature higher than the transition temperature $T_{1\mathbf{q}}^c$ of the single- \mathbf{q} state. This is one of the main results in this paper.

Finally, let us demonstrate the partially ordered configuration of quadrupoles in real space for the $zyox$ state. Since $\psi_0 = \mathbf{0}$, the direct substitution of $X_\ell = R_{zyox}^*/\sqrt{3} \equiv q^*/2$ and $\theta_\ell = \ell\omega$ into Eq. (33) leads to

$$\mathbf{Q}_A = \mathbf{0}, \quad \mathbf{Q}_B = q^* \hat{e}_\omega, \quad \mathbf{Q}_C = q^* \hat{e}_0, \quad \mathbf{Q}_D = q^* \hat{e}_{2\omega}, \quad (52)$$

where \hat{e}_θ is defined in Eq. (13). This is precisely what we have obtained in the microscopic calculations in Sec. V.

B. Instability to the $zyzx$ state

So far, we have only examined the antiferro orders of the modes of $\psi^{(\ell)}$ ($\ell = 1, 2, 3$). As shown in Sec. IV, they couple to the uniform moment $\psi^{(0)}$ in the single- \mathbf{q} and $zyzx$ ($zyzx'$) states. In the latter state, the order parameters consequently tilt from the directions $\theta_\ell = \ell\omega$. We will study this tilting in this section. To avoid complication in a full analysis, we employ an alternative approach based on a perturbation analysis of the mode coupling. We focus on the part of $K > -2J$. Thus, we consider the case where the order parameters are modified only slightly from the previous solutions in Sec. VII A. We restrict ourselves to the second-order stability analysis and show possible types of instability in each of the two states. We parametrize its small deformations as follows:

$$\mathbf{X} - R\bar{\mathbf{e}}_0 \sim \frac{1}{\sqrt{3}}R(-d_2\bar{\mathbf{e}}_1 + d_1\bar{\mathbf{e}}_2), \quad (53)$$

$$\boldsymbol{\theta} - \omega(1, 2, 0) \sim \eta_0\bar{\mathbf{e}}_0 + \eta_1\bar{\mathbf{e}}_1 + \eta_2\bar{\mathbf{e}}_2. \quad (54)$$

Here, the deformations $|d_j|$'s and $|\eta_j|$'s are all assumed to be small, and $\bar{\mathbf{e}}_0 = \frac{1}{\sqrt{3}}(1, 1, 1)$, $\bar{\mathbf{e}}_1 = \frac{1}{\sqrt{2}}(1, -1, 0)$, and $\bar{\mathbf{e}}_2 = \frac{1}{\sqrt{6}}(1, 1, -2)$.

The above small deviations from the $zyox$ state couple with the uniform moment $\psi_0 \equiv (\psi_{0u}, \psi_{0v})^T \equiv Q\hat{\mathbf{e}}_{\theta_\Gamma}$, and we also assume $Q \ll 1$. See Eqs. (13) and (34). The ψ_0 contributes to the free energy starting from the second-order term as $a_\Gamma(T)\psi_0^2 = a_\Gamma(T)Q^2$ with

$$a_\Gamma(T) \equiv \frac{1}{2}a_0(T) + J\gamma_0(\mathbf{0}) = \frac{1}{2}a_0(T) + 6J > a_X(T). \quad (55)$$

The couplings between ψ_0 and the deformation of the $zyox$ order parameters $|d_j|$'s and $|\eta_j|$'s arise from the following mode coupling terms $f_{\Gamma X} = f_{\Gamma X}^{(3)} + f_{\Gamma X}^{(4)}$, where

$$\begin{aligned} f_{\Gamma X}^{(3)} &= -\lambda \sum_{\ell=1}^3 [\psi_{0u}(\psi_u^{(\ell)2} - \psi_v^{(\ell)2}) - 2\psi_{0v}\psi_u^{(\ell)}\psi_v^{(\ell)}] \\ &= -\lambda Q \sum_{\ell=1}^3 X_\ell^2 \cos(2\theta_\ell + \theta_\Gamma), \end{aligned} \quad (56)$$

$$\begin{aligned} f_{\Gamma X}^{(4)} &= \lambda' \sum_{\ell < \ell'} [\psi^{(\ell)} \cdot \psi^{(\ell')}][\psi^{(6-\ell-\ell')} \cdot \psi_0] \\ &= \lambda' X_1 X_2 X_3 Q \sum_{\ell < \ell'} \cos(\theta_\ell - \theta_{\ell'}) \cos(\bar{\theta} - \theta_\ell - \theta_{\ell'} - \theta_\Gamma) \\ &= \lambda' X_1 X_2 X_3 Q \sum_{\ell=1}^3 \cos(2\theta_\ell + \theta_\Gamma - \bar{\theta}), \end{aligned} \quad (57)$$

where $\lambda \equiv 3b$ and $\lambda' \equiv 8c$. Collecting the terms within the second order in the deviations $d_{1,2}$, $\eta_{0,1,2}$, and ψ_0 in the free energy Eqs. (42), (56), and (57), one obtains the change in the free energy δf as

$$\begin{aligned} \delta f &\simeq \frac{1}{2}\alpha_0\eta_0^2 + \frac{1}{2}\alpha_1|\psi_0|^2 + \frac{1}{2}\alpha_2|\mathbf{d}|^2 + \frac{1}{2}\alpha_3|\boldsymbol{\eta}_\perp|^2 \\ &\quad - g_1\mathbf{d} \cdot \boldsymbol{\eta}_\perp - g_2\psi_0 \cdot \boldsymbol{\eta}_\perp + g_3\psi_0 \cdot \mathbf{d}. \end{aligned} \quad (58a)$$

Here, $\mathbf{d} \equiv (d_1, d_2)^T$ and $\boldsymbol{\eta}_\perp \equiv (\eta_1, \eta_2)^T$. The coefficients are given as

$$\alpha_0 = \frac{16}{3}KR^2 + 2\sqrt{3}bR^3, \quad \alpha_1 = 2a_\Gamma(T), \quad (58b)$$

$$\alpha_2 = \frac{2}{3}a_X(T)R^2 + \frac{2}{\sqrt{3}}bR^3 + \frac{4}{3}cR^4, \quad (58c)$$

$$\alpha_3 = \frac{16}{3}KR^2 + \frac{4}{3}c''R^4, \quad g_1 = \frac{4}{3}c''R^4, \quad (58d)$$

$$g_2 = \frac{\sqrt{2}}{3}R^2(\sqrt{3}\lambda - \lambda'R), \quad g_3 = \sqrt{\frac{2}{3}}\lambda R^2, \quad (58e)$$

We first note that the part of η_0 is decoupled in Eq. (58a) from the others, and the minimization leads to $\eta_0 = 0$ since $\alpha_0 > 0$. For discussing other diagonal coefficients α 's, let us assume $c = c' = c'' > 0$ as in the original form (39b). One notices that α_2 may change its sign with lowering temperature. The remaining α_1 and α_3 are positive, since we consider the situation of $a_\Gamma(T) > 0$ and $K > 0$. We denote by T_{α_2} the temperature at which $\alpha_2 = 0$. Then it is obtained by evaluating $a_X(T_{\alpha_2}) = -R_{zyox}^*(\sqrt{3}b + 2cR_{zyox}^*) < 0 = a_X(T_{1\mathbf{q}}^c)$, which shows $T_{\alpha_2} < T_{1\mathbf{q}}^c$. This value is $a_X(T_{\alpha_2}) = -63b^2/c$. Thus, ignoring the couplings g 's, one sees that the $zyox$ state is a locally stable solution for $T > T_{\alpha_2}$. We also note that g_2 [Eq. (58e)] may change its sign to negative as R increases.

The pure $zyox$ state becomes unstable, once δf in Eq. (58a) can take a negative value. A new stable configuration then acquires a nonvanishing value of one or some of ψ_0 , \mathbf{d} , and $\boldsymbol{\eta}_\perp$, which deform the original $zyox$ order. This instability is signaled by the appearance of a negative eigenvalue in the coefficient matrix. That is, the instability takes place at the position where the determinant D_3 of the block-diagonal 3×3 matrix changes from positive to negative. This determinant is given by

$$D_3 = \alpha_1\alpha_2\alpha_3 + 2g_1g_2g_3 - \sum_{i=1}^3 \alpha_i g_i^2. \quad (59)$$

Since Eq. (59) includes the effects of the coupling between $\psi^{(\ell)}$ and $\psi^{(0)}$, the condition of $D_3 = 0$ determines a transition temperature which is not necessarily the same as T_{α_2} .

Let us discuss this instability of the $zyox$ state but do it only qualitatively in order to simplify discussions. For large $K (> 0)$, it is natural to set $\boldsymbol{\eta}_\perp = \mathbf{0}$ in the zeroth-order approximation, since its coefficient α_3 is a large positive value. Analyzing the variations with ψ_0 and \mathbf{d} , we find that the $zyox$ state is unstable when $g_3^2 > \alpha_1\alpha_2$. Then, a nonvanishing deformation is spontaneously induced and it has the amplitude $\psi_0 = -C\mathbf{d}$ and $\boldsymbol{\eta}_\perp = C'\mathbf{d}$ with $C \sim g_3/\alpha_1 > 0$ and $C' \sim (g_1 - Cg_2)/\alpha_3$.

Suppose the induced ferro component ψ_0 points to the direction $\theta_\Gamma = 0$. This implies that the other induced deformations have the form of $d_1 < 0$ and $d_2 = \eta_2 = 0$. The sign of η_1 is also negative if $Cg_2 < g_1$ or positive otherwise. In our microscopic calculations, we have observed a wide region of the $zyzx$ state, which corresponds to the solution with deformation $\eta_1 < 0$. This is a consequence of the decrease of g_2 due to increasing R associated with lowering temperature. Although the transition

between $zyox$ and $zyzx$ states in Fig. 9(b) in the microscopic mean-field results is first order, the deformation is consistent with this analysis.

If ψ_0 is induced in the opposite direction $\theta_{\Gamma} = \pi$, the other induced deformation also changes their signs. $d_1 > 0$ with $\eta_1 > 0$ for $Cg_2 < g_1$. This is the $zyzx'$ state as shown in Fig. 10. See the second-order behavior in Fig. 11(c). Since the free energy (58a) fixes only the relative directions among ψ_0 , η_{\perp} , and \mathbf{d} , we cannot discuss the NS' state. The stability of the NS' state will be discussed in Sec. VII C.

C. Small K limit

So far, we have analyzed mostly the large- K region of the $K > 0$ part. The order parameters $\psi^{(\ell)}$ then point to the directions close to $\ell\omega$. We now analyze the opposite limit to see which types of orders are stabilized.

When K is small, the quadratic part of the free energy is nearly isotropic, and thus the quadrupole moments tend to rotate freely. This indicates that the three θ_{ℓ} 's can point to arbitrary directions under the constraint of $\cos \bar{\theta} = 1$ in the zeroth-order approximation. The details of this straightforward but lengthy analysis are explained for $K = 0$ in Appendix B. As shown in Fig. 16, three triple- \mathbf{q} states exist when $K = 0$. A set of three arrows schematically represent the antiferro moments $\{\psi^{(\ell)}\}_{\ell=1,2,3}$ in each state. In addition to the single- \mathbf{q} order, the phase diagram at $K = 0$ (see Fig. 18) has three regions of the triple- \mathbf{q} states: (i) symmetric triple- \mathbf{q} with $X_1 = X_2 = X_3$, (ii) uniaxial triple- \mathbf{q} with $X_1 = X_2 < X_3$, and (iii) fully-anisotropic triple- \mathbf{q} with X_{ℓ} 's all different. In each triple- \mathbf{q} state, only the relative directions of the order parameters $\theta_{\ell} - \theta_{\ell'}$ are fixed. This is because the eigenvalue of the exchange interaction for $K = 0$ in Eq. (12) is degenerate, $\Lambda_+(\mathbf{p}) = \Lambda_-(\mathbf{p})$ in Eq. (12), which means that the direction of the quadrupole moment $\psi^{(\ell)}$ can be arbitrary concerning the quadratic terms in the free energy. For example, a representative state for the symmetric triple- \mathbf{q} state (i) has $\boldsymbol{\theta} = (\omega, 2\omega, 0)$. By modifying this with all the permutations of θ_{ℓ} 's, one obtains other five states, which have the same energy as the original's. For the above (i), (ii), and (iii), the third and the fourth order terms determine the most stable one of the three. In the following, we will discuss how switching on K lifts this degeneracy.

First, let us examine the symmetric triple- \mathbf{q} states (i) for $K = 0$, which have the highest transition temperature and 24 domains. See Figs. 18 and 19. One of the domains corresponds to the $zyox$ state for $K > 0$ with $\boldsymbol{\theta} = (\omega, 2\omega, 0)$, and this was discussed in Sec. VII A. Note that this solution has four-fold degeneracy corresponding to different domains or equivalently disordered sublattice. For finite K , it is natural that the free energy of these four states becomes lower than those of the other states

in the symmetric triple- \mathbf{q} states.

As for the $zyzx$ state, its solution at $K = 0$ has a uniaxial anisotropy $X_1 = X_2 \neq X_3$. As demonstrated in Appendix B, the symmetric triple- \mathbf{q} state becomes unstable and is replaced by the uniaxial state at smaller values of a , which correspond to lower temperatures (Fig. 19). This has a configuration of the type $\boldsymbol{\theta} = (\frac{1}{2}\pi, -\frac{1}{2}\pi, 0)$, and we concentrate on this particular domain. For $K > 0$, the energy of the K -term is lowered for the configurations with $\theta_{\ell} \sim \ell\omega$. Because of $\theta_3 = 0$ in the above domain, one expects that the direction of $\psi^{(3)}$ does not tilt even for $K > 0$. In contrast, $\psi^{(1,2)}$ with $\theta_{1,2} = \pm\pi/2$ can tilt to lower the energy of the K -term for $K > 0$ with keeping $\bar{\theta} = 0$, $\theta_1 = -\theta_2 \sim \frac{1}{2}\pi + \delta \sim \frac{2}{3}\pi$ with $\delta > 0$. See a detailed analysis in Appendix C.

For the NS' state, one can perform a similar analysis starting from the fully-anisotropic state. However, since this reveals no new aspect, and so we omit its analysis here. We will return to these discussions about the anisotropic $zyzx$ and NS' states, when we analyze the NS state for $K < 0$ in Sec. VIII C.

VIII. ANALYSIS OF THE $K < 0$ PART

In the $K < 0$ part, the situation is more complicated, and we now perform its phenomenological analysis. This complication is due to the competition of the second- and third-order terms in the free energy (42). The minimum eigenvalue Λ_{\min} in Eq. (16) corresponds to the eigenvector, for example, $\mathbf{v}^+(\mathbf{k}_{\ell})$ and $\boldsymbol{\theta} = \pi(\frac{7}{6}, \frac{11}{6}, \frac{1}{2})$ as listed in Eq. (17). For the single- \mathbf{q} orders, the transition temperature is determined by $\tilde{a}_X(T) = 0$, where

$$\tilde{a}_X(T) \equiv \frac{1}{2}a_0(T) - 2J + 4K. \quad (60)$$

See Eq. (42). This satisfies $\cos \bar{\theta} = 0$ in Eq. (42), and this means no energy gain in the b -term. Therefore, one needs a full minimization to determine the order parameters to identify a stable state, and this requires solving coupled nonlinear equations with six variables. Instead of this elaborate work, we make a simple analysis in this section to explore an essential mechanism stabilizing the triple- \mathbf{q} orders for $K < 0$.

Recall that the b -term stabilizes the triple- \mathbf{q} states when $K > 0$. Thus we first examine whether the same mechanism works for $K < 0$. Assume that ψ_{ℓ} 's tilt slightly from the directions determined by minimizing the second-order term:

$$\boldsymbol{\theta} = \boldsymbol{\theta}_0 + (\delta_1, \delta_2, \delta_3), \quad \boldsymbol{\theta}_0 \equiv \pi(\frac{7}{6}, \frac{11}{6}, \frac{1}{2}). \quad (61)$$

Nonvanishing values of δ_{ℓ} 's do not minimize the second-order terms in the free energy, but some distorted triple- \mathbf{q} order may have a chance to lower the total free energy than that for the single- \mathbf{q} . This type of order with the three equivalent X_{ℓ} 's will be discussed in the section A

below. After that, in the following section B, we will also examine a configuration which can gain both of the b - and K -terms by introducing amplitude modulations in X_ℓ 's.

A. Case of $X_1 = X_2 = X_3$: the *zox*y state

It is natural to consider that a solution with the highest symmetry among the triple- \mathbf{q} states for $K < 0$ has a common amplitude of $\psi^{(\ell)}$'s ($X_1 = X_2 = X_3$) similarly to the *zyox* state for $K > 0$. This also leads to the constraint that δ_ℓ 's should be all the same in Eq. (61). Let us first examine this simplest case: $\delta_\ell = \alpha$ and $X_\ell = R/\sqrt{3}$ for all ℓ 's. This is the *zox*y state, and one of the four sublattices is disordered as in the *zyox* state. See also Eq. (71). Its free energy is given as

$$f_X = [\tilde{a}_X(T) - 8K \sin^2 \alpha] R^2 - \frac{2}{\sqrt{3}} b R^3 \sin 3\alpha + \frac{1}{4} c_2 R^4, \quad (62)$$

with $c_2 \equiv 4(c'' + 2c' + c)/3$. This has the symmetry $f_X(\pi - \alpha) = f_X(\alpha)$. Minimizing this with respect to α leads to the following two types of solutions:

$$\alpha_{\pm}^{(i)} = \frac{1}{2}\pi \pm \cos^{-1} \left[\sqrt{\frac{1}{4} + \bar{K}^2} + \bar{K} \right], \quad \text{for } K \leq 0, \quad (63a)$$

$$\alpha^{(ii)} = -\frac{1}{2}\pi, \quad \text{for } 0 \leq K, \quad (63b)$$

where $\bar{K} \equiv K/(\sqrt{3}bR)$ for $K < 0$ and this is a dimensionless parameter which controls the α -dependence, and $\bar{K} < 0$ for $K < 0$. The solution $\alpha^{(ii)}$ corresponds to the *zyox* state with $\theta = (\omega, 2\omega, 0)$ as discussed in Sec. VII A. However, since our concern is the region of $K < 0$ in this section, we do not consider that solution further.

The type (i) solutions exist for any $\bar{K} \leq 0$. Their range is $0 \leq \alpha_{-}^{(i)} \leq \frac{1}{6}\pi$, and $\alpha_{+}^{(i)} = \pi - \alpha_{-}^{(i)}$. The two solutions $\alpha_{\pm}^{(i)}$ have the same free energy, and we consider $\alpha_{-}^{(i)}$ for the moment. Its asymptotic form is $\alpha_{-}^{(i)} \sim (\sqrt{3}/8)|K|^{-1}bR$ for small $R/|K|$. Inserting this into Eq. (62), the corresponding free energy is obtained as

$$f_X^{(i)} = \tilde{a}_X(T)R^2 + \frac{1}{4}(c_2 + \frac{3}{2}K^{-1}b^2)R^4 + \dots \quad (64)$$

One should note that this has no R^3 -term. Therefore, if $c_2 + \frac{3}{2}K^{-1}b^2 > 0$, a possible transition must be continuous, and its transition temperature is given by the same expression $\tilde{a}_X(T) = 0$ [Eq. (60)] as that for the single- \mathbf{q} order. One can see this in Fig. 14 as a straight phase boundary with the *disordered* phase as J varies. Thus the fourth-order term determines which of the *zox*y or single- \mathbf{q} state appears. The free energy of the single- \mathbf{q} order is

$$f_X^{1\mathbf{q}} = \tilde{a}_X(T)R^2 + cR^4. \quad (65)$$

Comparing Eqs. (64) and (65), one obtains the appearance condition of the triple- \mathbf{q} state

$$4c > c_2 + \frac{3}{2}K^{-1}b^2 = \frac{4}{3}(c + 2c' + c'') - \frac{3}{2}(-K)^{-1}b^2. \quad (66)$$

For the parameters estimated from the local potential ($c = c' = c''$), this condition reads as

$$-\frac{9b^2}{8c} < K < 0. \quad (67)$$

This is consistent with the results of microscopic calculations in Fig. 9, which show the single- \mathbf{q} AFO₂₂ state for larger ($-K$). The transition can be first order, when the fourth-order coefficient $[c_2 - 3b^2/(-2K)]/4$ turns into negative for large b . However, its quantitative analysis needs to include fifth- and sixth-order terms in Eq. (39b). Using the expression (63a) in f_X , one sees that the free energy has a local minimum at $R = R_o$ with

$$R_o = c_2^{-1} \left\{ g + \sqrt{g^2 - 4c_2^2 \tilde{a}_X(T) [a_0(T) - 2J]} \right\}^{1/2}, \quad (68a)$$

$$g \equiv 6b^2 - 2c_2 [\tilde{a}_X(T) - 2K]. \quad (68b)$$

For $g < 0$, a second-order transition occurs at $\tilde{a}_X(T) = 0$. The condition $g < 0$ is indeed equivalent to the previous one $c_2 + \frac{3}{2}K^{-1}b^2 > 0$ derived from Eq. (64). For $g > 0$, the transition is generally first order. It occurs at the position where $f_X(R = R_1) = 0$, but we do not show the details. As discussed in Appendix B, the case of $K = 0$ turns out to be easier to analyze, and the results are much simpler. Indeed, those results are consistent with the microscopic mean-field calculations. See discontinuous behavior in Fig. 11(f), while continuous one in Fig. 11(h).

One can apply the above analysis to other cases with π shifts, which correspond to different domains. There are four different but equivalent domains in the same state, and their θ values are given as

$$\theta = \theta_0 + \alpha(1, 1, 1) + \{(0, 0, 0), (0, \pi, \pi), (\pi, 0, \pi), (\pi, \pi, 0)\}. \quad (69)$$

Here, α is the solution $\alpha_{-}^{(i)}$ in Eq. (63a) and $0 \leq \alpha \leq \frac{\pi}{6}$. Starting from any one of them, the other three can be obtained by translations as discussed in Sec. IV B. As for the solution $\alpha_{+}^{(i)} = \pi + \alpha = \pi - \alpha_{-}^{(i)}$ with $-\frac{\pi}{6} \leq \alpha \leq 0$ in Eq. (63a), one obtains

$$\theta = \theta_0 + \alpha(1, 1, 1) + \{(\pi, \pi, \pi), (\pi, 0, 0), (0, \pi, 0), (0, 0, \pi)\}. \quad (70)$$

The free energy for the latter sets (70) is identical to that for the former sets (69). Note the different ranges of the solution α for these two sets. In total, the *zox*y state has $8 = 4 \times 2$ domains; 4 corresponds to the trivial translations and 2 arises from the degeneracy related to the mirror operations with respect to one of Z_3 axes in the \mathbf{Q} space, e.g., $x \leftrightarrow y$, and $z \rightarrow z$. Note that the mirror symmetry is broken in the *zox*y states as shown in Fig. 9(d) and Fig. 10. Seeing Eq. (63a), one expects that $|\alpha|$ increases with lowering temperature, since R usually increases. This agrees qualitatively with the results of

microscopic calculations shown in Figs. 11(f) and 11 (h). As $|\alpha|$ approaches $\frac{1}{6}\pi$, the order parameters ψ_ℓ 's tilt their directions toward $\omega \times (\text{integer})$. This is similar to the $zyox$ state realized for $K > 0$, in which $\theta = (\omega, 2\omega, 0)$. In contrast, for the zox state, the directions θ approaches $(2\omega, 0, \omega)$, but this is not equivalent to *any* of the domains in the $zyox$ states. To see this, it is useful to check the real space configuration of the quadrupole moments. Since these configurations have no coupling to ψ_0 [Eqs. (56) and (57)], the uniform component vanishes $\psi_0 = \mathbf{0}$. Then, substituting $X_\ell = R/\sqrt{3} \equiv \bar{q}/2$ for all ℓ 's and $\theta = (2\omega, 0, \omega)$ into Eq. (33), one obtains

$$\mathbf{Q}_A = \mathbf{0}, \quad \mathbf{Q}_B = \bar{q}\hat{e}_{2\omega}, \quad \mathbf{Q}_C = \bar{q}\hat{e}_\omega, \quad \mathbf{Q}_D = \bar{q}\hat{e}_0. \quad (71)$$

This configuration indeed manifests a partial order. Compare this with Eq. (52). This agrees with the results of the microscopic calculations in Sec. V. See also Fig. 10 and Fig. 9(d). Note that this is the configuration corresponding to $\alpha = \frac{1}{6}\pi$. For general values of α , O_{22} -type components also mix as shown in Fig. 9. This is apparent since $\hat{e}_{\pi/2+\alpha} = \hat{e}_\omega \cos(\frac{\pi}{6} - \alpha) - \hat{e}_{\omega/4} \sin(\frac{\pi}{6} - \alpha)$. Here, \hat{e}_ω represents the O_{20} -type $(2x^2 - y^2 - z^2)$, while $\hat{e}_{\omega/4}$ does the O_{22} -type $(\sqrt{3}(z^2 - y^2))$.

B. Case of $X_1 = X_2 \neq X_3$: $zxzy$ state

Now, we study the states with an “ xzx ”-type anisotropy for $K < 0$. In addition to the high-symmetry solution with $X_1 = X_2 = X_3$ discussed in the previous section A, another simple way lowers the energy in both the K - and b -terms of f_X . This requires “uniaxial” modulations in the ψ_ℓ 's magnitude of quadrupole moments such as $X_1 = X_2 > X_3 > 0$. Here, the term “uniaxial” means that there is only one axis corresponding to the direction of $\psi^{(3)}$ around which the triple- \mathbf{q} configuration is symmetric in the quadrupole space as will be explained below. The directions θ are determined as follows. First, one expects that the free energy of the part of ψ_1 and ψ_2 in the K -term for $K < 0$ is lowered by setting $\theta_1 = -\theta_2 \sim \frac{7}{6}\pi$. Second, it is possible to lower f_X through the b term by setting $\theta_3 = 0$, since this satisfies $\bar{\theta} = 0$. An expectation is that the energy cost of the K -term is not large due to ψ_3 's small magnitude. This is indeed the $zxzy$ state obtained in Sec. IV B. Note that the trend is $\theta_1 \rightarrow \frac{7}{6}\pi$ as $K \rightarrow -\infty$. This choice of θ can lower both K - and b -terms of the free energy.

Let us concentrate on the case of large $(-K)$ in the following. The free energy reads

$$f_X^{zxzy} = 2\tilde{a}_X(T)X^2 + a_X(T)Z^2 - 6bX^2Z + c_3X^4 + c_4X^2Z^2 + cZ^4, \quad (72)$$

where $X \equiv X_1 = X_2$, $Z \equiv X_3$, $c_3 = 2(c + c') + c''$, and $c_4 = 4c' + 6c''$. The coefficients of the quadratic terms a_X and \tilde{a}_X were defined in Eqs. (44) and (60), respectively. Minimizing Eq. (72) with respect to X , we obtain

a stationary value of X and the result is

$$X = \left[\frac{-2\tilde{a}_X(T) + 6bZ - c_4Z^2}{2c_3} \right]^{1/2} \equiv X_*(Z). \quad (73)$$

Substituting this to Eq. (72), we obtain

$$f_X^{zxzy} = c_3^{-1} \left\{ [c_3a_X(T) - c_4\tilde{a}_X(T) - 9b^2]Z^2 - \tilde{a}_X^2(T) + 6\tilde{a}_X(T)bZ + 3c_4bZ^3 + (c_3c - \frac{1}{4}c_4^2)Z^4 \right\}. \quad (74)$$

The stationary value of Z is calculated via $\partial f_X^{zxzy}/\partial Z = 0$ with the constraint $X_*^2(Z) \geq 0$. Since its analytic solution is not so simple, we do not discuss the detail here. Nevertheless, it is certain that the transition between the $zyox$ and the $zxzy$ states is first-order, since it is determined by the crossing of their free energy values. One can also examine the stability of the $zxzy$ states in comparison with the lower symmetry NS state as has been done in Sec. VII B, but we do not show them here. Note that the above analysis neglects the ferro component ψ_0 . This is induced in the $zxzy$ state, and Eq. (72) is valid only for large $(-K)$. When $(-K)$ is very large, the moment directions are fixed to $\theta = \frac{7}{6}\pi(1, -1, 0)$ or one of the equivalent directions. However, at $K = 0$, as shown in Appendix B, the favored configurations are uniaxial ones, e.g., $\theta = \frac{3}{2}\pi(1, -1, 0)$, or its equivalent ones. This indicates that with decreasing $(-K)$, $|\theta_1|$ and $|\theta_2|$ decrease with keeping the symmetry of the $zxzy$ state. In the next section C, we will discuss the question whether such a $zxzy$ state survives for smaller $(-K)$.

The $zxzy$ state can break its symmetry down to that for the NS state with $X_1 \neq X_2 \neq X_3$. The phase transition is either first or second order. Once the three modes are inequivalent, the relation $|\theta_1| = |\theta_2|$ no longer holds. The discussion can be done in a similar way to that in Sec. VII B, but we omit it for simplicity. See the discussions in the next section C.

C. Fully asymmetric case: NS states

Lastly, we will discuss the no symmetry (NS) state. Instead of carrying out the stability analysis as has been done in the last sections A and B, we will take an alternative approach and study the limit of small $(-K)$. As discussed in Appendix B, some solutions at $K = 0$ have anisotropic configurations. These degenerate anisotropic states have different values of θ . Below, we will discuss how this degeneracy is lifted for $K < 0$.

Among the solutions at $K = 0$, the isotropic configuration shown in Fig. 16 obviously appears for $K < 0$ in a state connected to the zox state discussed in Sec. VIII A. At low temperatures, a wide range of the parameter space is covered by a phase with “ xzx ”-type uniaxial configurations and unbalanced magnitudes $X_1 = X_2 \neq X_3$. This is denoted by uniaxial triple- \mathbf{q} in Fig. 16. See detailed

discussions in Appendices C and D. They have the configurations of either $\mathbf{X} = (p, q, q)$ with $\boldsymbol{\theta} = \frac{1}{2}\pi(0, 1, -1)$ or $\mathbf{X} = (q, p, q)$ with $\boldsymbol{\theta} = \frac{1}{2}\pi(-1, 0, 1)$. We will investigate the possibility of tilting for the first case. To simplify our discussion, we assume that p and q are fixed. Representing the three modes of the tilting as $\delta\boldsymbol{\theta} = \alpha(1, 1, 1) + \delta(2, -1, -1) + \eta(0, 1, -1)$, the change in the K -term of the free energy is calculated up to the linear order as

$$\begin{aligned} \delta f_{2K}^{pqg}(\delta\boldsymbol{\theta}) &\sim 4\sqrt{3}K(p^2\delta\theta_X + q^2\delta\theta_Y) \\ &= 4\sqrt{3}K[(p^2 + q^2)\alpha + (2p^2 - q^2)\delta + q^2\eta]. \end{aligned} \quad (75)$$

Since the linear-order coefficients are nonvanishing above, these three modes are all induced, but the direction θ_3 is pinned to $-\frac{1}{2}\pi$ in this order. By taking account of other terms such as the cubic b terms, θ_3 may eventually tilt. Thus the uniaxial state becomes unstable for $K < 0$, and is replaced by the NS state.

This result partly explains the isolated island of the $xxzy$ state in the phase diagram shown in Fig. 9. The stability of the $xxzy$ state for large $(-K)$ depends on the free energy of the NS [Eq. (60)] and the single- \mathbf{q} [Eq. (65)] states. We do not try further analysis in this paper.

We close this section with a comment on a very small region where the configurations are $X_1 \neq X_2 \neq X_3$ and $\boldsymbol{\theta} = \frac{1}{2}\pi(0, 1, -1)$. This is denoted in Figs. 16 and 19 as the fully-anisotropic triple- \mathbf{q} for $K = 0$ and for small J . Since the three magnitudes differ to each other, the directions $\boldsymbol{\theta}$ tilt for finite K away from the directions $\boldsymbol{\theta} = \frac{1}{2}\pi(0, 1, -1)$, and this leads also to the NS (NS') state. Indeed, such changes have been observed in the microscopic calculations shown in Fig. 20(b).

IX. DISCUSSION

In this section, we discuss the implications of the present theory for the related materials including PrMgNi₄ and 5d¹ double perovskites. We also briefly comment on further implications of the multiple- \mathbf{q} physics of multipoles in other systems. It should be noted that the microscopic mean-field results in Sec. V based on the localized model are supported by the Landau analysis in Sec. VI. This indicates that the discussions about the triple- \mathbf{q} physics in this paper are also applicable to metallic systems. One should understand that the ordering wavevectors are determined with taking into account the effects of the conduction electrons.

A. Γ_3 quadrupole moments in real systems

The rare earth compound PrMgNi₄ has a structure in which Pr³⁺ ions form an fcc sublattice [16], and the CEF ground state of the Pr³⁺ ion has been identified

as the non-Kramers doublet Γ_3 . This material is metallic but shows no indication of the quadrupolar Kondo effects. For discussing the phase transition in this material, it is useful to compare it with the results obtained for the localized model. A detailed quantitative analysis needs more elaborate calculations and it is one of our future studies. The excited states of Pr³⁺ ion are the Γ_4 triplet at 1.16 meV, the Γ_1 singlet at 2.78 meV, and the Γ_5 triplet at 11.6 meV, and these excitation energies have been determined by the inelastic neutron scattering experiments [18]. Here, the excitation gap to Γ_1 corresponds to the parameter E_1 used in Eq. (10). Since the other states have no quadrupole matrix elements with the ground states Γ_3 , we have not taken them into account. The unidentified inelastic peaks at 2.5 and 5.9 meV suggest that the cubic lattice symmetry is weakly broken. However, thermodynamic experiments such as specific heat and magnetization measurements have shown no signature of phase transitions down to the temperature ~ 0.1 K. This broken lattice symmetry is now considered as an extrinsic effect of lattice imperfections or excess Mg atoms. They mask the intrinsic quadrupole ordering discussed in this paper, and thus further experimental studies using single crystals are necessary to identify the type of quadrupole order realized in this system. To explore exotic quadrupolar physics, it is important to find other materials related to PrMgNi₄. Mg or Ni may be replaced by nearby elements in the periodic table with similar chemical properties.

In a recent study, PrCdNi₄ was synthesized and found to show a clear phase transition [38]. The estimated entropy S at the transition temperature $T_q \simeq 1$ K is less than $\sim 0.5\ln 2$, and the ordering degrees of freedom have not been identified. A broad peak at $T \simeq 5$ K is reported in its specific heat above T_q . Although this might be a Schottky peak due to the CEF excited states, its origin remains unclear, since $S(T \simeq 5$ K) is less than $\ln 2$ and too small to conclude that this anomaly is due to the CEF excitations. In this respect, it is interesting to apply the present theory and explore a possibility of triple- \mathbf{q} ordered states above T_q . We have no information on the detailed bond dependence of the quadrupole exchange interactions, except the point that the total magnitude is about 1 K. In addition to the nearest-neighbor interactions, some further-neighbor ones may also be large and have non-negligible effects. For determining their values, it is useful to observe the spin-orbital wave in the ordered phase, and such experiments are highly desirable. We also expect that further experimental studies clarify the nature of the low temperature phase in PrCdNi₄.

Other interesting materials related to the present theory are the family of double-perovskites containing an fcc sublattice of ions with 5d¹ electron configuration [39–44]. A characteristic point is that those ions have a quartet ground state with the effective total angular momentum $J_{\text{eff}} = \frac{3}{2}$ due to strong spin-orbit coupling in 5d orbitals. Various nontrivial orders have been proposed for this system [45–47]. Under the cubic CEF, this quartet can be

regarded as a product state made of a spin- $\frac{1}{2}$ doublet and an orbital Γ_3 (E_g) doublet. Thus, in the temperature range where their spins remain disordered, we may expect that their orbital degrees of freedom are described by the present theory.

One member of this family is $\text{Ba}_2\text{MgReO}_6$. Hirai et al. studied it by synchrotron x-ray-diffraction measurement and observed a phase transition of the AFO_{22} -type quadrupole order at $T_q = 33$ K above the magnetic ordering temperature $T_m = 18$ K [43]. They also found a ferro O_{20} component below T_q , and it has been explained by considering the electron-lattice anharmonic coupling or lattice anharmonicity [43, 47, 48]. We propose to apply the present theory to this system and explain a ferro component as an induced moment due to the third-order coupling.

From our point of view, it is worthwhile to examine the effects of CEF excited states above the $J_{\text{eff}} = \frac{3}{2}$ multiplet on the magnitude of the observed ferro orbital moments. Important excited states are orbital singlet (spin doublet) states. They realize a situation of the orbital degrees of freedom similar to those studied in this paper, where the third-order couplings of quadrupoles take effects [49].

B. Other applications

We have demonstrated in this paper that the triple- \mathbf{q} quadrupole orders emerge generically, if not always, in the fcc lattice with nearest-neighbor interactions, and that some of them are partially ordered states. One of the main results is that the partial-order state for $K > 0$ (named *zoxy*) has a higher transition temperature than the single- \mathbf{q} quadrupole order. This is a consequence of the cooperation of the anisotropic interaction K and the third-order b -term of the local potential in the free energy. It is also important that the b term couples the modes at all the three X points, and this causes several triple- \mathbf{q} order patterns of quadrupoles. The translation symmetry imposes the important matching condition $\mathbf{k}_1 + \mathbf{k}_2 + \mathbf{k}_3 = \mathbf{G}$. Some three-dimensional systems have a set of high-symmetric \mathbf{k} -points in the Brillouin zone satisfying this condition. For example, $\mathbf{k}_1 = (0, \pi, \pi)$, $\mathbf{k}_2 = (\pi, 0, \pi)$, and $\mathbf{k}_3 = (\pi, \pi, 0)$ in a simple cubic lattice satisfy $\mathbf{k}_1 + \mathbf{k}_2 + \mathbf{k}_3 = \mathbf{G}$. In two dimensions, this condition is easily satisfied particularly in systems with a hexagonal symmetry, since the three vectors are confined in the same plane [50].

Multipoles have such third-order couplings, if their parity is even under both time reversal and spatial inversion operations. One can expect similar triple- \mathbf{q} orders in some other systems. For example, promising candidates are the system of electron t_{2g} orbitals (d_{xy} , d_{yz} , and d_{zx}) in cubic materials. Other candidates are those of the e_g orbitals in two- and three-dimensional systems. In the t_{2g} systems, a possible third-order coupling has a form of $\text{O}_{xy}\text{O}_{yz}\text{O}_{zx}$ [19], and this is similar to the b term

discussed in this paper.

We also note that such a third-order coupling also exists for composite degrees of freedom. For example, most natural candidates are the systems with both active dipole and quadrupole moments. This case was studied using the $R\text{Zn}$ compounds (R : rare earth element such as Tm or Nd) [51, 52] or actinide monopnictides [53], which have the CsCl-type crystal structure, i.e., an fcc structure. Recently, two of the present authors discussed that UNi_4B is also categorized to this type of materials [54]. It was motivated by the experiments pointing out the importance of quadrupole degrees of freedom in this system [55]. A triple- \mathbf{q} charge-density-wave (CDW) order has also been discussed for the kagome-lattice superconductors AV_3Sb_5 ($A = \text{K, Rb, Cs}$) [56–58]. Its free energy includes a cubic term similar to ours, and this also leads to triple- \mathbf{q} CDW orders in this system. This suggests an interesting possibility of superconductivity mediated by fluctuations in a triple- \mathbf{q} order, but this is not an issue of this paper and we do not discuss it further.

When a leading instability occurs at an incommensurate wavevector \mathbf{q} with small $|\mathbf{q}|$, this leads to several large-scale structures such as mosaic, (half-)vortex, or skyrmion, and this corresponds to triple- \mathbf{q} orders in magnetic systems [50]. We once again emphasize that those exotic configurations are stable at high temperatures as is the *zoxy* state in this paper. These fascinating possibilities will be examined in our future studies [59].

X. SUMMARY

In this paper, we have studied Γ_3 quadrupole orders in an fcc lattice. We have employed a four sublattice mean-field theory, and shown the presence of various triple- \mathbf{q} states, which include partially ordered states with disordered sites at high temperatures. We have discussed the stability of these states, based on the phenomenological Landau theory and shown that its results can well explain those of the microscopic mean-field calculations. The third-order coupling of quadrupoles in the free energy plays a crucial role for stabilizing the triple- \mathbf{q} states with the ordering vectors located at the zone boundary X points. This unique mechanism for the triple- \mathbf{q} orders is quite ubiquitous in the systems with the time-reversal even parity including electric multipoles, and it also works in many other systems. We believe that our work stimulates further theoretical studies and experiments on exotic quadrupole or other multipole orders in future.

ACKNOWLEDGMENT

This work was supported by JSPS KAKENHI (Grant Nos. JP16H04017, JP18K03522, and JP21H01031).

Appendix A: Detail Analysis on the Large K limit for $K > 0$

We start with minimizing the free energy f_X in Eq. (42) with respect to the following two angle variables Θ and Φ with $0 \leq \Theta, \Phi \leq \pi/2$ in two steps:

$$(X, Y, Z) = R(\sin \Theta \cos \Phi, \sin \Theta \sin \Phi, \cos \Theta). \quad (\text{A1})$$

We will see that an important dimensionless parameter is

$$y \equiv \frac{3b}{c_1 R} > 0. \quad (\text{A2})$$

The first step is the minimization with respect to Φ . Calculation of $\partial f_X / \partial \Phi$ leads to the condition $\sin^4 \Theta \cos 2\Phi [\sin 2\Phi - \sigma(\Theta)/\sigma(\Theta_c)] = 0$ with $\sigma(x) \equiv \cos x / \sin^2 x$. Here, $\Theta_c = \Theta_c(y)$ is defined as

$$\Theta_c(y) = \cos^{-1}[\sqrt{1+y^2} - y]. \quad (\text{A3})$$

Note that $\Theta_c(y)$ is a monotonically increasing function, and $\Theta_c(0) = 0$ and $\Theta_c(y \rightarrow \infty) = \pi/2$. An important relation is $\cos \Theta_c(y_\star) = y_\star$ at the special value $y_\star = 1/\sqrt{3}$. Judging also from the corresponding values of second-order derivative, the minima are located at

$$\Phi^* = \begin{cases} \pi/4, & (\text{for } 0 \leq \Theta \leq \Theta_c) \\ \Phi_2, \pi/2 - \Phi_2, & (\text{for } \Theta_c \leq \Theta \leq \pi/2) \end{cases} \quad (\text{A4})$$

with

$$\Phi_2(\Theta) = \frac{1}{2} \sin^{-1} \left[\frac{\sigma(\Theta)}{\sigma(\Theta_c)} \right]. \quad (\text{A5})$$

The case of $\Theta = 0$ corresponds to the single- \mathbf{q} state, which is not under consideration here. For these obtained Φ^* values in Eq. (A4), we further examine the extremum and minimum conditions with respect to Θ .

For $\Phi = \pi/4$, the extremum condition is $0 = \partial f_X / \partial \Theta \propto \sin \Theta (3 \cos^2 \Theta - 1)(\cos \Theta - t)$. Therefore, there is at most one minimum and it is located at $\Theta_\star = \cos^{-1} y_\star$ for $y > y_\star$. The energy of this local minimum is

$$f_X \left(\Theta_\star, \Phi^* = \frac{\pi}{4} \right) = \left(y^{-1} - \frac{2}{\sqrt{3}} \right) b R^3, \quad (\text{A6})$$

and this is negative when $y > \sqrt{3}/2$. This solution corresponds to the symmetric triple- \mathbf{q} state with $X = Y = Z$. The case of $0 < y < y_\star$ has no minimum in this Θ -region.

For $\Theta_c < \Theta < \pi/2$, the minimum in the Φ -direction at $\Phi^* = \pi/4$ splits into two minima located at $\Phi_2(\Theta)$ and $\pi/2 - \Phi_2(\Theta)$. The extremum condition with respect to Θ is

$$\left. \frac{\partial f_X}{\partial \Theta} \right|_{\Phi=\Phi_2(\Theta)} \propto \sin(2\Theta) [t^2 + \cos(2\Theta)], \quad (\text{A7})$$

for both of the two new positions. Therefore a local minimum exists only when $y < 1$ and its position is

the symmetric point $\Theta^* = \pi/2$. The other extremum points (Θ^*, Φ^*) are located at $\Theta^* = (1/2) \cos^{-1}(-y^2)$ or $\pi - (1/2) \cos^{-1}(-y^2)$ and $\Phi^* = \Phi_2(\Theta^*)$ or $\pi/4 - \Phi_2(\Theta^*)$, but they are all saddle points, because they are local maxima in the Θ -direction.

Let us summarize the results for the local minima of $f_X(\Theta, \Phi)$. Their locations depend on the value of t and

$$(\Phi^*, \Theta^*) = \begin{cases} (\Phi^*, 0), (0, \frac{\pi}{2}), (\frac{\pi}{2}, \frac{\pi}{2}), & \text{for } 0 < t < t_\star, \\ (\frac{\pi}{4}, \cos^{-1} t_\star), & \text{for } t < t^* < 1 \end{cases} \quad (\text{A8})$$

Note that Φ^* is arbitrary when $\Theta^* = 0$.

There are two classes of stationary solutions. One is single- \mathbf{q} configurations. The other is symmetric triple- \mathbf{q} ($zyox$) state with $X = Y = Z = R/\sqrt{3}$. The free energy for the single- \mathbf{q} reads

$$f_X^{1\mathbf{q}} = a_X(T) R^2 + c R^4, \quad (\text{A9})$$

while that for the $zyox$ configuration is

$$f_X^{zyox} = a_X(T) R^2 - \frac{2b}{\sqrt{3}} R^3 + \left(c + \frac{1}{3} c_1 \right) R^4. \quad (\text{A10})$$

Here, $a_X(T)$ is defined in Eq. (44). Equation (A10) shows that the $zyox$ state is stabilized by the third-order term, while the magnitude of the fourth-order term depends on the anisotropic coupling c' and c'' according to the definition of c_1 in Eq. (47).

Appendix B: Analysis of the $K = 0$ case: effects of the local free energy

We analyze in this Appendix the triple- \mathbf{q} orders at $K = 0$. The isotropic J term alone contributes to the inter-site interaction part of the free energy f_X in Eq. (42) as $(\frac{1}{2} a_0 - 2J) R^2$. This analysis is qualitatively the same as that for the local free energy, since the cubic and the fourth-order terms in the free energy arise from the local CEF potential and the form of the quadratic part is isotropic. Thus, the stable states at $K = 0$ can be regarded as those favored by the single-ion potential. For complete analysis, it is necessary to take into account the effect of anisotropic inter-site interactions, i.e., the K -term. Nevertheless it is very useful to analyze the properties of the states favored by the single-ion potential. By using this knowledge as a starting point, we perform a stability analysis at $K \neq 0$ in Secs. VII and VIII.

1. Minimization with respect to θ_i 's

First, we minimize f_X in Eq. (42) with respect to the order parameter directions $\theta_{X,Y,Z}$. Their amplitudes are assumed to be known. Ignoring the quadratic K -term

proportional to K , one can write down the free energy as a sum of the following four terms.

$$f_X = f_X^{24} + f_X^3 + f_X^{4A} + f_X^{4B}. \quad (\text{B1a})$$

With the notation of $\mathbf{X} = (X_1, X_2, X_3) = (X, Y, Z)$ and $\boldsymbol{\theta} = (\theta_1, \theta_2, \theta_3) = (\theta_X, \theta_Y, \theta_Z)$, two of the four terms do not depend on θ_i 's: $f_X^{24} = a(T)R^2 + cR^4$ and $f_X^{4A} = 2\Delta c \sum_{i < j} X_i^2 X_j^2$, where $a(T) = \frac{1}{2}a_0(T) - 2J$ and $\Delta c = c' - c$, and $R^2 = \sum_i X_i^2$ as before. The other two terms do depend as

$$f_X^3 = -6b X_1 X_2 X_3 \cos \bar{\theta}, \quad \left(\bar{\theta} = \sum_i \theta_i\right), \quad (\text{B1b})$$

$$f_X^{4B} = 4c'' \sum_{i < j} X_i^2 X_j^2 \cos^2 \theta_{ij}, \quad (\theta_{ij} \equiv \theta_i - \theta_j). \quad (\text{B1c})$$

We can assume without any loss of generality the relation $X_1 \geq X_2 \geq X_3$, and we will examine this case. As for the order parameter directions, the free energy depends on their three combinations, $\bar{\theta}$, θ_{13} and θ_{23} . Note that they constitute a complete set of the directions, since $\theta_{12} = \theta_{13} - \theta_{23}$. The $\bar{\theta}$ -dependence immediately shows the minimum is located at $\bar{\theta}^* = 0$.

Therefore, in order to minimize with respect to θ_{ij} 's, it is convenient to consider the function $\bar{f} \equiv f_X^{4B} / (4c'' X_1^2 X_2^2) = A \cos^2 \theta_{23} + B \cos^2 \theta_{13} + \cos^2(\theta_{23} - \theta_{13})$, where the coefficients are

$$A \equiv \left(\frac{X_3}{X_1}\right)^2 \leq B \equiv \left(\frac{X_3}{X_2}\right)^2 \leq 1, \quad (\text{B2})$$

and their ratio is denoted as

$$\kappa \equiv \frac{A}{B} = \left(\frac{X_2}{X_1}\right)^2 \leq 1. \quad (\text{B3})$$

See Fig. 17(a). Because of the symmetries $\bar{f}(\theta_{23}, \theta_{13}) = \bar{f}(\theta_{23} + \pi, \theta_{13}) = \bar{f}(\theta_{23}, \theta_{13} + \pi) = \bar{f}(-\theta_{23}, -\theta_{13})$, it suffices to consider the fundamental region, $(\theta_{23}, \theta_{13}) \in (-\pi/2, \pi/2] \times [0, \pi/2]$. The symmetric points $(\theta_{23}, \theta_{13}) = \frac{\pi}{2}(n_2, n_1)$ are local extrema for any integers n_2 and n_1 irrespective of the values of A and B , but most of them are maxima or otherwise saddle points. In the fundamental region, $(0, \pi/2)$ is the only point among them which has a chance of being minimum. We calculated the \bar{f} 's Hessian and found that this local minimum is stable as far as $A \leq B/(1+B) \equiv A_c(B)$. Note that the upper bound A_c cannot exceed $1/2$. When A increases beyond $A_c(B)$ with B fixed, the local minimum at $(0, \pi/2)$ becomes unstable and starts to move towards the direction proportional to $-(B, A_c(B))$. The minimum position $(\theta_{23}^*, \theta_{13}^*)$ is determined by solving the extremum conditions

$$\sin[2(\theta_{23}^* - \theta_{13}^*)] = -A \sin(2\theta_{23}^*) = B \sin(2\theta_{13}^*). \quad (\text{B4})$$

If $A_c(B) < A \leq B$, one and only one solution exists *inside* the fundamental region, and this is a minimum position of \bar{f} . Its explicit expression reads as

$$\theta_{23}^* = -\frac{1}{2}\pi + \frac{1}{2}\sin^{-1}[\mathcal{S}/(2\kappa A)], \quad (\text{B5a})$$

$$\theta_{13}^* = \frac{1}{2}\pi - \frac{1}{2}\sin^{-1}[\mathcal{S}/(2\kappa B)], \quad (\text{B5b})$$

$$\mathcal{S} \equiv \left\{ [1 - (\kappa - A)^2] \left[(A/A_c(B))^2 - 1 \right] \right\}^{1/2}. \quad (\text{B5c})$$

Since $(\kappa - A)^2 < 1$, this result once again manifests that this nontrivial solution exists only when $A > A_c(B)$. For evaluating the free energy, we need the values of $\cos^2 \theta_{ij}$'s. We have calculated them from Eq. (B5) and found that their expressions are particularly simple in terms of X_j :

$$\cos^2 \theta_{ij}^* = [R^2/(2X_i^2) - 1][R^2/(2X_j^2) - 1], \quad (\text{B6})$$

where $R^2 = \sum_i X_i^2$ as defined before. Thus, the minimum value $f_X^{4B*} = 4c'' X_1^2 X_2^2 \bar{f}(\{\theta_{ij}^*\})$ is immediately calculated with these values, and the result is

$$f_X^{4B*} = \begin{cases} 4c'' X_2^2 X_3^2, & \text{when } R/\sqrt{2} < X_1 \\ c'' \left(R^4 - 2 \sum_i X_i^4 \right), & \text{otherwise.} \end{cases} \quad (\text{B7})$$

Here, X_1 and X_3 should be understood as the largest and smallest respectively of $\{X, Y, Z\}$ in general cases, while X_2 is the remaining one. The condition for the upper case is equal to the previous one $A < A_c(B)$.

Let us now determine the values of θ_i 's from the above results. In order to obtain all the possibilities, one should also consider the solutions not limited to the fundamental region $\pm(\theta_{23}^*, \theta_{13}^*) + \pi(n_2, n_1)$. Combining the result for $\bar{\theta}$, one finds the minimum positions are represented as $\boldsymbol{\theta}^* = (\theta_1^*, \theta_2^*, \theta_3^*) = n_0 \omega \mathbf{d}_0 + \frac{2}{3}[(\pm\theta_{13}^* + n_1\pi)\mathbf{d}_1 + (\pm\theta_{23}^* + n_2\pi)\mathbf{d}_2]$ where the two plus-minus signs should take an identical value. The vectors \mathbf{d}_0 , \mathbf{d}_1 , and \mathbf{d}_2 are $(1, 1, 1)$, $(1, -\frac{1}{2}, -\frac{1}{2})$, and $(-\frac{1}{2}, 1, -\frac{1}{2})$, respectively. The representative value $(\theta_{23}^*, \theta_{13}^*)$ is the symmetric point $(0, \pi/2)$ for $A < A_c(B)$, or the nontrivial solution (B5) for $A > A_c(B)$. Counting independent combinations, one finds 24 different sets of $(\theta_1^*, \theta_2^*, \theta_3^*)$ for a general value of $(\theta_{23}^*, \theta_{13}^*)$, but all of them can be generated from one representative $\boldsymbol{\theta}^{*\circ}$ using three types of symmetry operations. They are

$$(i) \text{ inversion: } \theta_i^* \rightarrow \frac{2}{3}\bar{\theta} - \theta_i^*, \text{ for } \forall i, \quad (\text{B8a})$$

$$(ii) \text{ mirror: } \theta_i^* \rightarrow \theta_i^*, \theta_j^* \rightarrow \theta_j^* + \pi, \text{ for } j \neq i, \quad (\text{B8b})$$

$$(iii) \text{ rotation: } \theta_i^* \rightarrow \theta_i^* \pm \omega, \text{ for } \forall i. \quad (\text{B8c})$$

The total number of the combinations is indeed $(1+1) \times (1+3) \times (1+2) = 24$. For the trivial minimum point $(\theta_{23}^*, \theta_{13}^*) = (0, \pi/2)$ for $A \leq A_c(B)$, the number is reduced to 12, since the half of the operations duplicate the points. One may choose $\boldsymbol{\theta}^{*\circ} = (\pi/2)(0, 1, -1)$ as a representative for this case. One should note that for the half of the 12 sets two θ_i 's are identical. This is a consequence of one of the mirror operations. When \bar{f} has no anisotropy ($A = B = 1$), the value of nontrivial solution is $(\theta_{23}^*, \theta_{13}^*) = \omega(-\frac{1}{2}, \frac{1}{2})$, and there also exist 24 minimum points of $\boldsymbol{\theta}^*$. Six of them have a symmetric 120° -configuration $\{\theta_1^*, \theta_2^*, \theta_3^*\} = \{-\omega, 0, \omega\}$, while the others have an umbrella configuration $\{\theta_1^*, \theta_2^*, \theta_3^*\} = \{(n - \frac{1}{2})\omega, n\omega, (n + \frac{1}{2})\omega\}$.

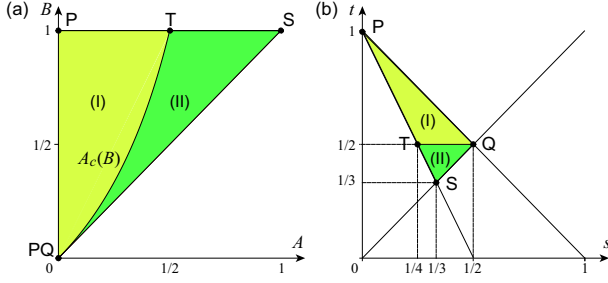


FIG. 17. (a) Parameters in the renormalized free energy \tilde{f} . Special points in the panel (b) are also shown. Note that the point P there corresponds to the edge connecting $(A, B) = (0, 0)$ and $(0, 1)$. The colored two parts are the region under consideration. They are separated by the boundary $A = A_c(B)$, where the minimum position of \tilde{f} starts to shift from $(\theta_{23}, \theta_{13}) = (0, \frac{\pi}{2})$. (b) Domain of the dimensionless free energy $\tilde{g}^{34}(t, s)$. The fundamental region ($X_3 \leq X_2 \leq X_1$) is colored.

2. Minimization with respect X_i 's

Now that f_X has been minimized with respect to the order parameter directions $\{\theta_i\}$, the next minimization procedure is about their amplitudes $\{X_i\}$. As before, we do this under the constraint of $\sum_i X_i^2 = R^2$ being fixed. The simplest way of imposing this constraint is the use of the parametrization $X_1^2 = R^2 t$, $X_2^2 = R^2 s$, and $X_3^2 = R^2(1 - s - t)$, and we search a minimum point in the (s, t) -space. Since the free energy is invariant upon any permutation of $\{X_i\}$, it suffices to consider the fundamental region illustrated in Fig. 17 (b), which corresponds to the part of $X_3 \leq X_2 \leq X_1$.

For minimization with respect to s and t , it suffices to consider the following dimensionless function \tilde{g}^{34} , since f_X^{24} is independent of s and t :

$$\tilde{g}^{34}(t, s) \equiv \frac{f_X^3 + f_X^{4A} + f_X^{4B*}}{bR^3} = \tilde{g}^3 + \bar{c}_A \tilde{g}^{4A} + \bar{c}_B \tilde{g}^{4B}, \quad (\text{B9a})$$

$$\tilde{g}^3 = -6[ts(1 - s - t)]^{1/2}, \quad (\text{B9b})$$

$$\tilde{g}^{4A} = 2[t + s - (t + s)^2 + ts] =: \mathcal{W}(t, s), \quad (\text{B9c})$$

$$\tilde{g}^{4B} = \begin{cases} 4s(1 - s - t) & \text{for } t \geq \frac{1}{2}, \\ 2\mathcal{W}(t, s) - 1 & \text{for } t < \frac{1}{2}, \end{cases} \quad (\text{B9d})$$

with the coefficients scaled as

$$\bar{c}_A \equiv \Delta c R / b, \quad \bar{c}_B \equiv c'' R / b. \quad (\text{B9e})$$

Note that its domain is a narrow region shown in Fig. 17 (b), and its control parameters are only \bar{c}_A and \bar{c}_B . As for \tilde{g}^{4A} , its minimum and maximum locate at the P and S point, respectively: $\tilde{g}^{4A}(P) = 0$ and $\tilde{g}^{4A}(S) = \frac{2}{3}$. As for \tilde{g}^{4B} , the local maximum value is $\tilde{g}^{4B}(T) = \frac{1}{4}$ and $\tilde{g}^{4B}(S) = \frac{1}{3}$ in the region I and II, respectively. Its minimum is degenerate and $\tilde{g}_{\min}^{4A} = 0$ at all the points on the edge PQ.

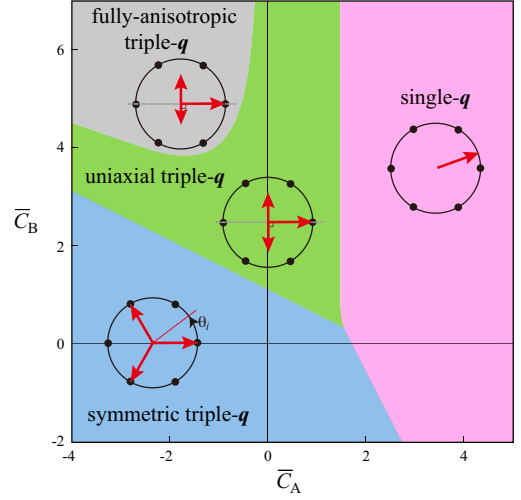


FIG. 18. Configurations of the order parameters at the X points in the parameter space of \bar{c}_A and \bar{c}_B defined in Eq. (B9e) for $K = 0$. Arrows represent three vectors $\psi_{\mathbf{k}_\ell}$. The fully-anisotropic state is not realized at $\bar{c}_A = 0$ ($c = c' = c''$). In the single- \mathbf{q} state, the arrow can freely rotate, since the free energy has no anisotropy with respect to its direction in Eq. (B1a).

Therefore, numerical minimization of \tilde{g}^{34} is easy to perform with searching the entire domain, and we have determined the phase diagram covering the main part of the parameter space. The result is shown in Fig. 18, and the minimum position $(t_\#, s_\#)$ differs among the four parts marked by different colors.

First, the red part (large- \bar{c}_A region) is the single- \mathbf{q} state, since the minimum locates at the point $(t_\#, s_\#) = (1, 0)$ corresponding to $\mathbf{X} = (R, 0, 0)$.

Secondly, the blue part (region of negatively large \bar{c}_A) is the symmetric triple- \mathbf{q} state, and the minimum locates at the symmetric position $(t_\#, s_\#) = (\frac{1}{3}, \frac{1}{3})$ corresponding to $X_1 = X_2 = X_3 = \frac{R}{\sqrt{3}}$. The minimum position does not move within each of these two states. Therefore, the transition between them is first order, and the border is given by the line $2\bar{c}_A + \bar{c}_B = 2\sqrt{3}$.

Thirdly, in the green-color part the minimum point locates on the edge PT in the domain, and thus the solution has an uniaxial symmetry ($X_2 = X_3 < \frac{R}{2} < \frac{R}{\sqrt{2}} < X_1$). As \bar{c}_A decreases, the single- \mathbf{q} state (red part) becomes unstable and continuously turns into this state. This phase boundary is determined by a breakdown of the stability condition of the minimum at the P point, and this gives the vertical line $\bar{c}_A = \frac{3}{2}$. However, this continuous transition terminates at the tricritical point $(\bar{c}_A^*, \bar{c}_B^*) = (\frac{3}{2}, \frac{3}{4})$, and the transition becomes first order for $\bar{c}_B < \bar{c}_B^*$. The first order transition line slightly winds and connects to the end point of the boundary between the single- \mathbf{q} and symmetric triple- \mathbf{q} states $(\bar{c}_A^{**}, \bar{c}_B^{**}) = (1.567, 0.330)$. The symmetric triple- \mathbf{q} state (blue part) also becomes unstable and turns into the uniaxial state, as \bar{c}_B increases. The minimum at the S point becomes unstable on the line

$\bar{c}_A + 2\bar{c}_B = 3\sqrt{3}/2$. However, a first-order transition takes place before that and the minimum jumps to a point with $t_\# > \frac{1}{2}$. This determines the boundary of the symmetric and uniaxial triple- \mathbf{q} states.

Lastly in the gray part, the minimum of \bar{g}^{34} locates *inside* the triangle PTQ, and thus the solution has no symmetry corresponding to fully-anisotropic triple- \mathbf{q} state. This also means that the transition to the uniaxial triple- \mathbf{q} state is continuous.

This phase diagram of \bar{g}^{34} in Fig. 18 is actually very useful, and we can make many predictions based on it for possible phase transitions in the f_X system upon lowering temperature. In any ordered state, the order parameter amplitude R is nonvanishing and varies with T . Usually, $R(T)$ grows as T decreases. When the disordered phase changes to an ordered state, $R(T)$ varies continuously starting from 0 if the transition is continuous, while jumps to a finite value otherwise. In any case, the two parameters \bar{c}_A and \bar{c}_B vary with T according to Eq. (B9e) with $R = R(T)$, but *they are confined on a ray* starting from the origin, i.e., \bar{c}_B/\bar{c}_A is independent of T . Therefore, we can predict which ordered states may appear upon temperature control by looking at the changes on the ray in Fig. 18. By repeating this procedure with varying the ray's direction $u = \tan^{-1} \bar{c}_B/\bar{c}_A$, we can determine the phase diagram.

Let us write down explicitly the above procedure. Suppose a set of parameters a , b , and c 's is given, and consider possible phase transitions upon lowering temperature. The first step is the construction of the following function:

$$\bar{g}_u(R) \equiv \bar{g}^{34}(t_\#, s_\#) \Big|_{\bar{c}_A = RC \cos u, \bar{c}_B = RC \sin u}, \quad (\text{B10})$$

where the two dimensional vector $b^{-1}(2\Delta c, c'')$ is parameterized by its modulus C and angle u . Here, $(t_\#, s_\#)$ denotes the minimum position for the given value of R . The total free energy density is then given as

$$\tilde{f}_X = a(T)R^2 + cR^4 + bR^3\bar{g}_u(R). \quad (\text{B11})$$

Now, the Landau free energy functional has been minimized with respect to all the degrees of freedom except for R . Therefore, the minimization with respect to R is the last task. The minimum is determined by the stationary condition $d\tilde{f}_X/dR = 0$, but it always has the trivial solution $R = 0$. A nontrivial solution is the one satisfying the following equation:

$$-2a(T) - 4cR^2 = 3bR\bar{g}_u(R) + bR^2 \frac{d\bar{g}_u(R)}{dR} =: \mathcal{U}_u(R^2). \quad (\text{B12})$$

One can solve this graphically: plot \mathcal{U}_u as a function $\rho \equiv R^2$ and find its crossing with the straight line $-2a(T) - 4c\rho$. If it crosses from below as ρ increases, its crossing point $\rho_\star(T)$ determines the minimum position as $R = \sqrt{\rho_\star(T)}$. If there are multiple crossing points of this kind, the one with the lowest \tilde{f}_X is the global minimum. Then, the stable state at the temperature T is that in Fig. 18 at the position $(\bar{c}_A, \bar{c}_B) = \sqrt{\rho_\star(T)}C(\cos u, \sin u)$.

Appendix C: Detail of small K analysis

In this Appendix, we examine how a finite value of K affects the anisotropic configurations at $K = 0$. Using the previous notation $\mathbf{X} = (X_1, X_2, X_3)$ for (X, Y, Z) and $\boldsymbol{\theta} = (\theta_1, \theta_2, \theta_3)$ for $(\theta_X, \theta_Y, \theta_Z)$, the K -term in the free energy f_X in Eq. (42) reads as

$$f_{2K}^{X_1 X_2 X_3}(\theta_1, \theta_2, \theta_3) = -4K \sum_{j=1}^3 X_j^2 \cos(2\theta_j + j\omega), \quad (\text{C1})$$

where $\omega \equiv \frac{2}{3}\pi$ as before. Let us start discussing from the limit of $K = 0$. There are three equivalent configurations: $(\mathbf{X}, \boldsymbol{\theta}) = (q, q, p, \frac{\pi}{2}, -\frac{\pi}{2}, 0)$ and its two equivalents $(p, q, q, 0, \frac{\pi}{2}, -\frac{\pi}{2})$, and $(q, p, q, -\frac{\pi}{2}, 0, \frac{\pi}{2})$. They are indeed realized at low temperatures at $K = 0$ as discussed in Appendix B2. Upon switching on K , the degeneracy of these three configurations is lifted as is evident from the factor $\cos(2\theta_j + j\omega)$ appearing in Eq. (C1). This will result in different behavior in their stability.

Before discussing the effects of $f_{2K}^{X_1 X_2 X_3}$, we first check the stability of the $K = 0$ solution against rotating the order parameters. Let us consider small variations in the order parameter directions such that $\pm\frac{\pi}{2} \rightarrow \pm\frac{\pi}{2} + \eta_\pm$ and $0 \rightarrow \eta_0$. Then, the corresponding change in the free energy δf_X is calculated by evaluating Eq. (42)

$$\delta f_X|_{K=0} \sim q^2 \left[3bp(\eta_+ + \eta_- + \eta_0)^2 + 2c''p^2(\eta_+ + \eta_- - 2\eta_0)^2 + 2c''(p^2 - 2q^2)(\eta_+ - \eta_-)^2 \right]. \quad (\text{C2})$$

The leading term in this change is quadratic with respect to the three sets of linear combinations of η_\pm and η_0 . They are the eigenmodes within this harmonic approximation, and their energies are all positive, since $p^2 \geq 2q^2$ for these states and b is assumed positive. This concludes that the solution at $K = 0$ is stable against small variations in $\boldsymbol{\theta}$.

Now we calculate $f_{2K}^{X_1 X_2 X_3}$'s for the aforementioned three configurations. The results are

$$f_{2K}^{qqp}(\frac{\pi}{2}, -\frac{\pi}{2}, 0) = -4K(p^2 + q^2), \quad (\text{C3a})$$

$$f_{2K}^{pqq}(0, \frac{\pi}{2}, -\frac{\pi}{2}) = f_{2K}^{qpq}(-\frac{\pi}{2}, 0, \frac{\pi}{2}) = 2K(p^2 + q^2). \quad (\text{C3b})$$

Thus, for $K > 0$, the configuration $\boldsymbol{\theta} = (\frac{1}{2}\pi, -\frac{1}{2}\pi, 0)$ is the most stable, while those with $(0, \frac{1}{2}\pi, -\frac{1}{2}\pi)$ or $(-\frac{1}{2}\pi, 0, \frac{1}{2}\pi)$ are stabilized for $K < 0$. To simplify the discussion, we restrict ourselves to the analysis of $f_{2K}^{X_1 X_2 X_3}$ with fixing $X_1 = X_2 = q$ and $X_3 = p$, and consider a free energy change δf_{2K}^{qqp} associated with small variations in $\boldsymbol{\theta}$. For $K > 0$, straightforward calculation gives

$$\delta f_{2K}^{qqp}(\frac{\pi}{2} + \eta_+, -\frac{\pi}{2} + \eta_-, \eta_0) \sim 4K [2p^2\eta_0^2 + q^2(\eta_+^2 + \eta_-^2) - \sqrt{3}q^2(\eta_+ - \eta_-)]. \quad (\text{C4a})$$

The stability of this configuration is examined by minimizing the sum of this δf_{2K}^{qqp} and $\delta f_X|_{K=0}$ in Eq. (C2).

It is important that this δf_{2K} has a linear term of $\eta_+ - \eta_-$. Therefore, its nonvanishing amplitude is induced as $\eta_+ - \eta_- \sim \sqrt{3}K/[c''(p^2 - 2q^2)]$, while the other two eigenmodes remain zero in their amplitudes. This indicates that the two directions θ_1 and θ_2 tilt from $\pm \frac{1}{2}\pi$ but the relation $\theta_1 = -\theta_2$ continues to hold.

For $K < 0$, similar analyses show that a linear term appears once again in $\delta f_{2K}^{X_1 X_2 X_3}$

$$\begin{aligned} & \delta f_{2K}^{pq}(\eta_0, \frac{\pi}{2} + \eta_+, -\frac{\pi}{2} + \eta_-) \\ & \sim 4|K|[p^2\eta_0^2 + q^2(2\eta_-^2 - \eta_+^2) - \sqrt{3}(q^2\eta_+ + p^2\eta_0)], \quad (C4b) \end{aligned}$$

$$\begin{aligned} & \delta f_{2K}^{qp}(-\frac{\pi}{2} + \eta_-, \eta_0, \frac{\pi}{2} + \eta_+) \\ & \sim 4|K|[p^2\eta_0^2 + q^2(2\eta_+^2 - \eta_-^2) + \sqrt{3}(q^2\eta_- + p^2\eta_0)]. \quad (C4c) \end{aligned}$$

The linear term is proportional to $q^2\eta_{\pm} + p^2\eta_0$, and this combination contains at least two or generally all the three eigenmodes in Eq. (C2). Therefore, these eigenmodes acquire nonvanishing values in the configuration minimizing the total δf_X . The values of η_{\pm} and η_0 are thus nonvanishing, and generally they have no symmetry. This further induces inequivalent changes in the magnitudes $\{X_j\}$. Therefore these configurations with no symmetry correspond to NS states for $K < 0$. A final remark is about a negative coefficient of one of η_{\pm}^2 in Eqs. (C4b) and (C4c). Since this is proportional $|K|$, one can neglect their effects, as in the case of $K > 0$, as far as $|K|$ is small.

Appendix D: Phase changes across the $K = 0$ line

In this Appendix, we study in detail how various symmetry broken phases change near the $K = 0$ line in the (J, K) parameter space based on the results of the microscopic mean-field approximation in Sec. IV. In particular, we focus on the region of very low temperature. As shown in the inset of Fig. 9 (c), the NS' state exists near the $K = 0$ line. Its phase boundary with the $zyzx$ state touches the $K = 0$ line around $J/E_1 \sim 0.007$, and indeed the touching point is $J_c/E_1 \simeq 0.0067$ at $T = 0$. The ground state for $J > J_c$ is the uniaxial triple- \mathbf{q} state shown in Fig. 18, while it is the fully-anisotropic state for $0 < J < J_c$. For $J < 0$, the ground state is always the ferro state, but this is not our interest in this paper. In this Appendix, we use the notations $\mathbf{X} = (X, Y, Z)$ and $\boldsymbol{\theta} = (\theta_X, \theta_Y, \theta_Z)$.

Figure 19 shows the J - T phase diagram at $K = 0$. The color map represents the magnitude difference ΔQ between the smallest and the second smallest ones among X , Y , and Z . This is one type of the order parameter identifying the fully-anisotropic state, where the three magnitudes are all different. The region with finite ΔQ is limited to a small part of $J > 0$ at low temperatures. In the part of $J > 0$, the phase with the highest transition temperature is the symmetric triple- \mathbf{q} state as discussed in Appendix B. Its lower T side is covered by the uniaxial triple- \mathbf{q} state with “ xzx ” anisotropy.

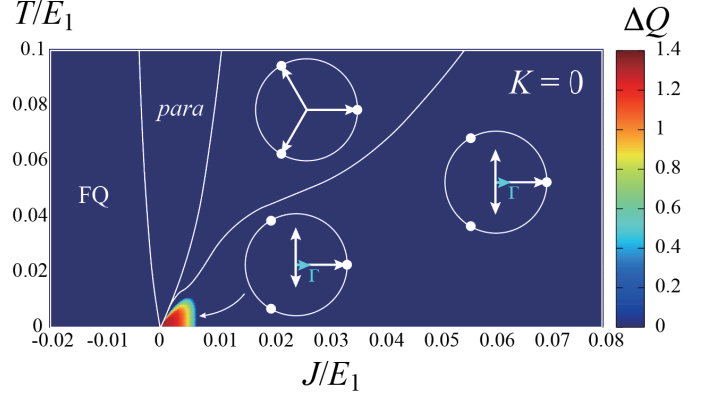


FIG. 19. Color plot of ΔQ in J - T plane for $K = 0$. ΔQ is finite only in the fully-anisotropic state for $0 < J < J_c$. The phase boundaries are indicated by the white lines and for the triple- \mathbf{q} states, the quadrupole configurations in the wavenumber space are schematically shown.

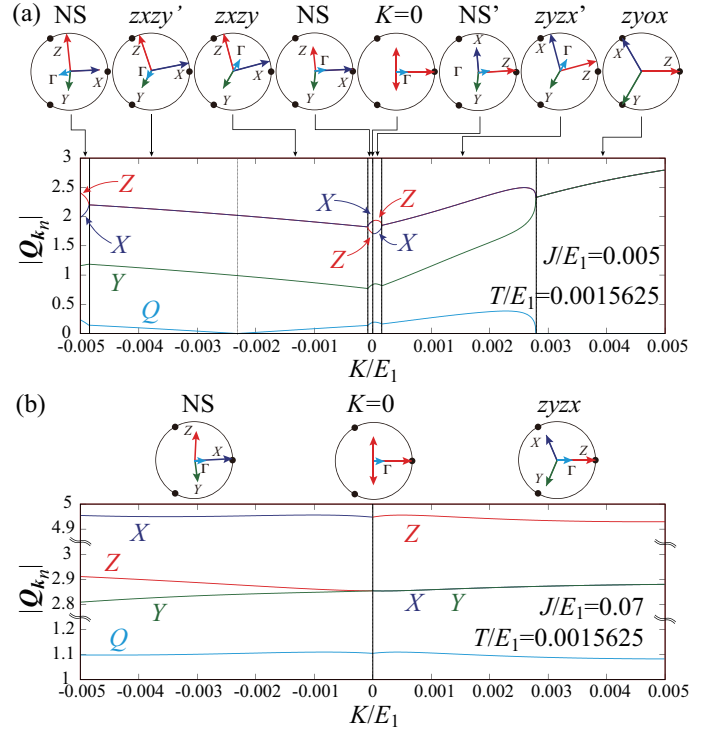


FIG. 20. $|Q_{k_n}|$ as a function of K near $K = 0$. (a) $J/E_1 = 0.005$, where the ground state for $K = 0$ is the fully-anisotropic state with $X \neq Y \neq Z$. (b) $J/E_1 = 0.07$, where the ground state for $K = 0$ is the uniaxial state with $X = Y \neq Z$. The order parameters for $K \rightarrow 0+$ and $K \rightarrow 0-$ are different but they belong to the equivalent domains in the order parameters for $K = 0$. In each of the figure, schematic configurations $\{Q_{k_n}\}$ are drawn for the intuitive understanding about the changes in the order parameters.

At $K = 0$, the ordered states have many equivalent

domains. Once K becomes finite, these degeneracies are lifted, and some of them are stabilized. Figure 20 shows the change of $|\mathbf{Q}_{k_0}|$ and $\{|\mathbf{Q}_{k_\ell}|\}_{\ell=1}^3 = \{X, Y, Z\}$ upon varying K with J fixed. The temperature is set to $T = 0.0015625$, practically equivalent to $T = 0$. The two panels correspond to the results for different J 's: $J/E_1 =$ (a) 0.005 and (b) 0.007. The phase at $K = 0$ is the fully-anisotropic state in the panel (a), and the uniaxial state in the panel (b).

Let us start with discussing the $K = 0$ case in the panel (a) of Fig. 20. The three magnitudes X , Y , and Z are all different. The configuration of one typical domain there is schematically illustrated: the magnitude is the largest for that with $\theta = 0$, and the smallest for $\theta = -\pi/2$. This state is degenerate in its configuration, and this degeneracy corresponds to 36 different domains except for trivial translations. First, there are $3!$ ways of assigning \mathbf{Q}_{k_ℓ} 's to these three vectors, and the corresponding 6 permutations constitute a first class. There are two other classes of operations generating degenerate domains. One type of operation is the direction exchange $\pi/2 \leftrightarrow -\pi/2$ while the direction for the largest moment is fixed at $\theta = 0$. The other type is the rotation $\theta \rightarrow \theta \pm \omega$ for all the moments. Combining these three types of operations yield in total $3! \times (1 + 1) \times (1 + 2) = 36$ domains, and they are degenerate in the fully-anisotropic triple- \mathbf{q} state at $K = 0$.

The degeneracy of these 36 domains is lifted when $K \neq 0$. In Fig. 20(a), we show the configuration where the smallest magnitude is Y and its direction is $\theta_Y \sim -\pi/2$. Upon switching on $K > 0$, the configuration with $Z \geq X > Y$ is stabilized, since $\theta_Z \sim 0$ ensures the *maximum gain* in the quadratic terms in f_X . At the same time, $\theta_X = \pi/2$ and $\theta_Y = -\pi/2$, and they are quite close to ω and $-\omega$, respectively, which also lowers f_X . In contrast, for $K < 0$, the moment with the two larger magnitudes X and Z point to the direction $\theta_X \sim \pi/6$ and $\theta_Z \sim \pi/2$. This *maximizes the energy gain* in the quadratic terms in f_X . As for the smallest one Y , it points to the direction $\theta_Y = -\omega$, which *mini-*

mizes the energy cost in f_X , while *maximizes the energy gain* in the b -term. See the discussion in Sec. VIII B. Irrespective of the sign of K , the phase changes with K as $\text{NS} \rightarrow \text{zxzy} \rightarrow \text{NS}$ and $\text{NS}' \rightarrow \text{zyzx}' \rightarrow \text{zyox}$. These changes are accompanied by rotations of the moments, which are smooth but quite complicated. It should be noted that the appearance of the zyzx' and $\text{zxzy}'(\text{zxzy})$ states is related to the topological transition of the local mean-field state as discussed in Sec. III. One of the quadrupole moments, say \mathbf{Q}_A , is pinned to $\mathbf{Q}_A = (-1, 0)$ in the “spin-1/2” regime. Without symmetry breaking to NS or NS', \mathbf{Q}_A cannot vary continuously within the “half-integer spin” regime. See also Fig. 15.

Let us switch to the panel (b) of Fig. 20. The uniaxial triple- \mathbf{q} state is realized at $K = 0$. The configurations shown are for the domain in which the moment for $\theta = 0$ has the largest magnitude among the 36 degenerate domains.

The stability of the uniaxial triple- \mathbf{q} state has been analyzed in Secs. VII C, VIII B, and VIII C, and in Appendix C. There we have demonstrated that the NS' state does not appear for $K > 0$, while the NS state does appear for $K < 0$. One can see this in the mean-field calculations in Fig. 20(b). Note that, when considering the instability of the fully-anisotropic triple- \mathbf{q} state, the NS' state can appear as shown in the inset of Fig. 9(c). The configurations shown are those with Y being the smallest magnitude. For $K > 0$, one of the previously degenerate domains at $K = 0$ gradually transforms into the zyzx state. During this process, the moment with the largest magnitude Z keeps the directions $\theta_Z = 0$, while the other two with the same magnitude $X = Y$ tilt their directions θ_X and θ_Y . For the parameter space shown in the panel (b), the largest moment is that for X for $K < 0$ owing to the quadratic terms f_X . Note that we consider the situation with Y being the smallest. The two smaller magnitude Z and Y start to vary differently; Z increases while Y decreases with lowering $K (< 0)$. This is the NS state and the angles $\theta_{X,Y,Z}$ also tilt from the directions at $K = 0$.

-
- [1] Y. Tokura and N. Nagaosa, *Science* **288**, 462 (2000).
 - [2] Y. Zhou, K. Kanoda, and T.-K. Ng, *Rev. Mod. Phys.* **89**, 025003 (2017).
 - [3] M. Fiebig, T. Lottermoser, D. Meier, and M. Trassin, *Nature Reviews Materials* **1**, 16046 (2016).
 - [4] J. A. Mydosh and P. M. Oppeneer, *Philosophical Magazine* **94**, 3642 (2014).
 - [5] J. Nasu, M. Udagawa, and Y. Motome, *Phys. Rev. Lett.* **113**, 197205 (2014).
 - [6] B. Kim, H. Ohsumi, T. Komesu, S. Sakai, T. Morita, H. Takagi, and T. H. Arima, *Science* **323**, 1329 (2009).
 - [7] G. Jackeli and G. Khaliullin, *Phys. Rev. Lett.* **102**, 017205 (2009).
 - [8] H. Takagi, T. Takayama, G. Jackeli, G. Khaliullin, and S. E. Nagler, *Nature Reviews Physics* **1**, 264 (2019).
 - [9] S. Hayami, M. Yatsushiro, Y. Yanagi, and H. Kusunose, *Phys. Rev. B Condens. Matter* **98**, 165110 (2018).
 - [10] M. Yatsushiro, H. Kusunose, and S. Hayami, *Phys. Rev. B Condens. Matter* **104**, 054412 (2021).
 - [11] K. Hattori and H. Tsunetsugu, *J. Phys. Soc. Jpn.* **83**, 034709 (2014).
 - [12] K. Hattori and H. Tsunetsugu, *J. Phys. Soc. Jpn.* **85**, 094001 (2016).
 - [13] T. Ishitobi and K. Hattori, *J. Phys. Soc. Jpn.* **88**, 063708 (2019).
 - [14] T. Onimaru and H. Kusunose, *J. Phys. Soc. Jpn.* **85**, 082002 (2016).
 - [15] H. Tsunetsugu, T. Ishitobi, and K. Hattori, *J. Phys. Soc. Jpn.* **90**, 043701 (2021).
 - [16] Y. Kusanose, T. Onimaru, G.-B. Park, Y. Yamane, K. Umeo, T. Takabatake, N. Kawata, and T. Mizuta, *J. Phys. Soc. Jpn.* **88**, 083703 (2019).

- [17] Y. Kusanose, T. Onimaru, G.-B. Park, Y. Yamane, K. Umeo, and T. Takabatake, JPS Conf. Proc. **30**, 011160 (2020).
- [18] Y. Kusanose, T. Onimaru, Y. Yamane, K. Umeo, T. Takabatake, T. Guidi, D. Le, and D. T. Adroja, J. Phys. Conf. Ser. **2164**, 012052 (2022).
- [19] A. V. Nikolaev and K. H. Michel, Eur. Phys. J. B **9**, 619 (1999).
- [20] M. B. Walker, C. Kappler, K. A. McEwen, U. Steigenberger, and K. N. Clausen, J. Phys.: Condens. Matter **6**, 7365 (1994).
- [21] T. Ishitobi and K. Hattori, Phys. Rev. B **104**, L241110 (2021).
- [22] S. Lee, S. Trebst, Y. B. Kim, and A. Paramekanti, Phys. Rev. B **98**, 134447 (2018).
- [23] F. Freyer, J. Attig, S. Lee, A. Paramekanti, S. Trebst, and Y. B. Kim, Phys. Rev. B **97**, 115111 (2018).
- [24] F. Freyer, S. Lee, Y. B. Kim, S. Trebst, and A. Paramekanti, Phys. Rev. Research **2**, 033176 (2020).
- [25] A. Sakai and S. Nakatsuji, J. Phys. Soc. Jpn. **80**, 063701 (2011).
- [26] K. Matsubayashi, T. Tanaka, A. Sakai, S. Nakatsuji, Y. Kubo, and Y. Uwatoko, Phys. Rev. Lett. **109**, 187004 (2012).
- [27] T. Taniguchi, K. Hattori, M. Yoshida, H. Takeda, S. Nakamura, T. Sakakibara, M. Tsujimoto, A. Sakai, Y. Matsumoto, S. Nakatsuji, and M. Takigawa, J. Phys. Soc. Jpn. **88**, 084707 (2019).
- [28] S. Kittaka, T. Taniguchi, K. Hattori, S. Nakamura, T. Sakakibara, M. Takigawa, M. Tsujimoto, A. Sakai, Y. Matsumoto, and S. Nakatsuji, J. Phys. Soc. Jpn. **89**, 043701 (2020).
- [29] S. Sachdev, Quantum Phase Transitions (Cambridge University Press, New York, 2011).
- [30] R. Shiina, H. Shiba, and P. Thalmeier, J. Phys. Soc. Jpn. **66**, 1741 (1997).
- [31] H. Kusunose and Y. Kuramoto, J. Phys. Soc. Jpn. **74**, 3139 (2005).
- [32] V. P. Mineev and M. E. Zhitomirsky, Phys. Rev. B **72**, 014432 (2005).
- [33] K. Kugel and D. I. Khomskii, Zh. Exsp. Thor. Fiz. **64**, 369 (1973), Sov. Phys. JETP **37**, 725 (1973).
- [34] K. Kubo and T. Hotta, Phys. Rev. B **95**, 054425 (2017).
- [35] B. A. Bernevig and L. H. Taylor, Topological Insulators and Topological Superconductors (Princeton University Press, Princeton, 2013).
- [36] F. D. M. Haldane, Phys. Lett. A **93**, 464 (1983).
- [37] F. D. M. Haldane, Phys. Rev. Lett. **50**, 1153 (1983).
- [38] Y. Kusanose and T. Onimaru, unpublished.
- [39] S. S. Erickson, S. Misra, G. J. Miller, R. R. Gupta, Z. Shlesinger, W. A. Harrison, J. M. Kim, and I. R. Fisher, Phys. Rev. Lett. **99**, 016404 (2007).
- [40] M. A. de Vries, A. C. McLaughlin, and J.-W. G. Bos, Phys. Rev. Lett. **104**, 177202 (2010).
- [41] L. Lu, M. Song, W. Liu, A. P. Reyes, P. Kuhns, H. O. Lee, I. R. Fisher, and V. F. Mitrović, Nat. Commun. **8**, 14407 (2017).
- [42] S. Gao, D. Hirai, H. Sagayama, H. Ohsumi, Z. Hiroi, and T.-H. Arima, Phys. Rev. B **101**, 220412 (2020).
- [43] D. Hirai, H. Sagayama, S. Gao, H. Ohsumi, G. Chen, T.-h. Arima, and Z. Hiroi, Phys. Rev. Research **2**, 022063 (2020).
- [44] H. Arima, Y. Oshita, D. Hirai, Z. Hiroi, and K. Matsubayashi, J. Phys. Soc. Jpn. **91**, 013702 (2022).
- [45] G. Chen, R. Pereira, and L. Balents, Phys. Rev. B **82**, 174440 (2010).
- [46] D. Churchill and H.-Y. Kee, Phys. Rev. B **105**, 014438 (2022).
- [47] C. Svoboda, W. Zhang, M. Randeria, and N. Trivedi, Phys. Rev. B **104**, 024437 (2021).
- [48] N. Iwahara and L. F. Chibotaru, (2022), arXiv:2211.09577 [cond-mat.str-el].
- [49] H. Kubo, T. Ishitobi, and K. Hattori, Phys. Rev. B **107**, 235134 (2023).
- [50] T. Okubo, S. Chung, and H. Kawamura, Phys. Rev. Lett. **108**, 017206 (2012).
- [51] P. Morin, J. Rouchy, and D. Schmitt, Phys. Rev. B Condens. Matter **17**, 3684 (1978).
- [52] M. Amara, P. Morin, and P. Burlet, Physica B **210**, 157 (1995).
- [53] G. H. Lander and P. Burlet, Physica B **215**, 7 (1995).
- [54] T. Ishitobi and K. Hattori, Phys. Rev. B **107**, 104413 (2023).
- [55] T. Yanagisawa, H. Matsumori, H. Saito, H. Hidaka, H. Amitsuka, S. Nakamura, S. Awaji, D. I. Gorbunov, S. Zherlitsyn, J. Wosnitza, K. Uhlířová, M. Vališka, and V. Sechovský, Phys. Rev. Lett. **126**, 157201 (2021).
- [56] B. R. Ortiz, L. C. Gomes, J. R. Morey, M. Winiarski, M. Bordelon, J. S. Mangum, I. W. H. Oswald, J. A. Rodriguez-Rivera, J. R. Neilson, S. D. Wilson, E. Ertekin, T. M. McQueen, and E. S. Toberer, Phys. Rev. Materials **3**, 094407 (2019).
- [57] Y.-X. Jiang, J.-X. Yin, M. M. Denner, N. Shumiya, B. R. Ortiz, G. Xu, Z. Guguchia, J. He, M. S. Hossain, X. Liu, J. Ruff, L. Kautzsch, S. S. Zhang, G. Chang, I. Belopolski, Q. Zhang, T. A. Cochran, D. Multer, M. Litskevich, Z.-J. Cheng, X. P. Yang, Z. Wang, R. Thomale, T. Neupert, S. D. Wilson, and M. Z. Hasan, Nat. Mater. **20**, 1353 (2021).
- [58] M. M. Denner, R. Thomale, and T. Neupert, Phys. Rev. Lett. **127**, 217601 (2021).
- [59] K. Hattori, T. Ishitobi, and H. Tsunetsugu, unpublished.